



An Operational Thermodynamic-Dynamic Model for the Coastal Labrador Sea Ice Melt Season

Ian D. Turnbull¹, and Rocky S. Taylor^{1,2}

¹C-CORE

²Memorial University of Newfoundland (MUN)

Corresponding author: Ian Turnbull (ian.turnbull@card-arctic.ca)

7

1 C-CORE

Captain Robert A. Bartlett Building

1 Morrissey Road

St. John's, Newfoundland and Labrador A1B 3X5 Canada

Ian Turnbull Phone: (709)-864-6208

Fax: (709)-864-4706

14

2 Memorial University of Newfoundland

Faculty of Engineering and Applied Science

S.J. Carew Building

240 Prince Philip Drive

St. John's, Newfoundland and Labrador A1B 3X5 Canada

Rocky Taylor Phone: (709)-864-4370

Fax: (709)-864-4706

E-mail: rocky.taylor@card-arctic.ca



23 Abstract

24 An offshore operations thermodynamic-dynamic prediction model of sea ice break-up and drift is presented for
25 central coastal Labrador in Atlantic Canada, and demonstrated for portions of the 2015 spring break-up of the land-
26 fast ice. The model validation is performed using the data from ice tracking buoys deployed on the land-fast ice,
27 which began drifting after break-up of the land-fast ice. The model uses a one-dimensional thermodynamic
28 parameterization for ice melt and growth, includes snow accumulation and melt, and melt-pond and lead growth and
29 contraction. The dynamic model uses a Smoothed Particle Hydrodynamics (SPH) parameterization for ice motion
30 and changes in ice thickness and concentration. The dynamic forcing parameters include wind and ocean current
31 drag, Coriolis deflection, internal ice stresses, and gravitational forcing due to sea surface gradients. A coastal
32 repulsion force is employed to prevent ice particles from crossing the coastal boundaries. The model is sensitive to
33 the prescribed initial snow depth on the sea ice. In the present work, analysis of results is focused on the offshore
34 regions of Makkovik and Nain, Labrador. The melt of the coastal land-fast ice in these regions can be adequately
35 simulated by the thermodynamic model alone. The model predicts the timing of the local land-fast ice break-up to
36 within 4.6 hours to six days, and can simulate observed ice buoy drift speeds to within 1.5 meters per second.

37 1 Introduction

38 Sea ice forecast models are an important tool for offshore industries operating in ice-prone environments, such as
39 those involved in hydrocarbon exploration and development or marine transport. Accurate pack ice model forecasts
40 allow for operations to be planned for maximum safety, efficiency, and minimum downtime as operators make the
41 best possible preparations for the anticipated ice conditions, and can develop an advance understanding of how those
42 conditions and associated hazards are likely to evolve during operations. While small-scale models are useful for
43 generating drift forecasts for single or several ice floes over spatial scales of up to tens of km, regional and basin-
44 scale models provide forecasts of ice conditions on scales of tens to hundreds of km, and permit operators to develop
45 a picture of changes in ice conditions over such a broad area in which vessels and drilling platforms may travel.
46 Such forecast models are useful for generating ice forecasts on timescales of days to months.

47 In this paper, a model is presented to simulate the melt and break-up of the land-fast ice along the central Labrador
48 coast during the spring break-up season, as well as the regional ice dynamics in the further offshore marginal ice
49 zone (MIZ). The model is designed to be an operational planning and ice forecast tool for the offshore oil and gas
50 industry, as well as the marine transport industry. It is designed to accept gridded metocean input parameters from
51 numerical weather prediction and ocean models. The model simulations presented here are run for selected periods
52 during April-May 2015, and are compared to in-situ observations of ice drift as recorded by tracking buoys deployed
53 on ice floes, and to reanalysis data on ice thickness, concentration, and velocity as provided by the Operational
54 Mercator global Ocean analysis and forecast system. The models runs are forced with atmospheric and precipitation
55 reanalysis data from the North American Regional Reanalysis (NARR), the European Center for Medium Range
56 Weather Forecasting (ECMWF), and with ocean model output from the Operational Mercator global Ocean analysis
57 and forecast system.

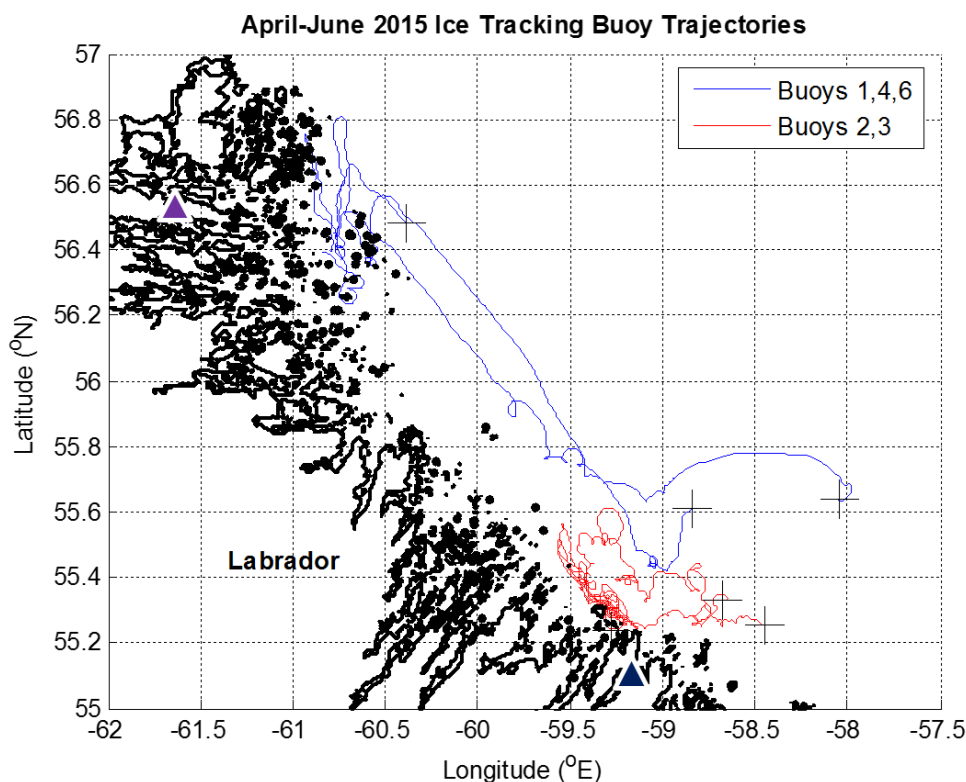


58 The results presented here focus particularly on the regions offshore Makkovik and Nain, Labrador, as these
59 locations have been identified as economically important for vessel transit. Makkovik has been identified as a
60 potential landing site for a pipeline from oil and gas fields offshore Labrador, and Nain is located near the port of
61 Edward's Cove which serves the Voisey's Bay nickel mine (Vale, 2015). In this paper, two locations offshore
62 Makkovik and Nain are selected to demonstrate the thermodynamic model simulation of the melt and break-up of
63 the land-fast ice during April 1 – May 31, 2015. Results from the thermodynamic model are also presented for the
64 central coastal Labrador region from Makkovik to Nain. Subsequently, the coupled thermodynamic-dynamic model
65 is demonstrated for the Makkovik-Nain region for May 1-7, 2015, which coincides with the break-up of the land-fast
66 ice offshore Nain.

67 1.1 Ice tracking buoy deployments

68 On April 9, 2015, six Iridium satellite-tracked buoys were deployed toward the outer edge of the land-fast ice
69 offshore Labrador (see Figure 1). The buoys were dropped out of a Twin Otter fixed-wing airplane, and were
70 deployed in two triangular arrays offshore Makkovik and Nain. These buoy deployments served to collect data on
71 the precise timing of the land-fast ice break-up at these locations during the 2015 melt season, and the subsequent
72 drift patterns of the broken floes. Table 1 summarizes the offshore deployment areas for the six buoys and the time
73 periods over which they drifted on ice following the break-up of the land-fast ice on which they were deployed. The
74 on-ice drift periods were determined from analysis of the internal temperatures transmitted by the buoys, as the on-
75 ice periods were characterized by distinctly larger diurnal temperature fluctuations in response to air temperatures,
76 compared with more homogeneous temperature records once the buoys fell into open water. The open water drift of
77 the buoys is not considered in this paper.

78 Buoys 1, 4, and 6 were deployed offshore Nain, and buoys 2, 3, and 5 were dropped offshore Makkovik. The first
79 drift motion recorded by the buoys took place on April 23 offshore Makkovik, and on May 1 offshore Nain. Buoy 5
80 failed on May 28 on the land-fast ice offshore Makkovik and never recorded any movement (Table 1).



81

82 **Figure 1.** Trajectories of six ice tracking buoys offshore Labrador during April 23 – June 12, 2015. The dark blue
 83 and purple white-outlined triangles mark the locations of Makkovik and Nain, respectively. The black plus (+)
 84 symbols mark the ends of the buoys' on-ice drift trajectories.

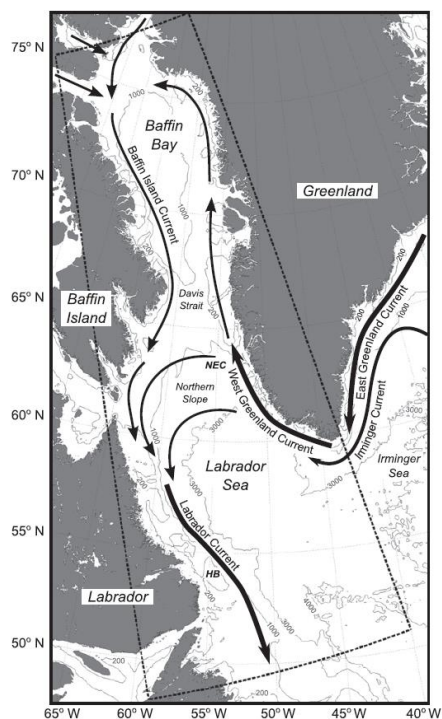
85 **Table 1.** Deployment areas and time periods over which the six ice buoys drifted on ice following the break-up of
 86 the land-fast ice.

Buoy	Deployment Area	Ice Drift Period
1	Nain	May 1-18
2	Makkovik	April 23 – June 12
3	Makkovik	April 23 - June 8
4	Nain	May 2-11
5	Makkovik	N/A
6	Nain	May 6-19

87 **1.2 Regional environment**

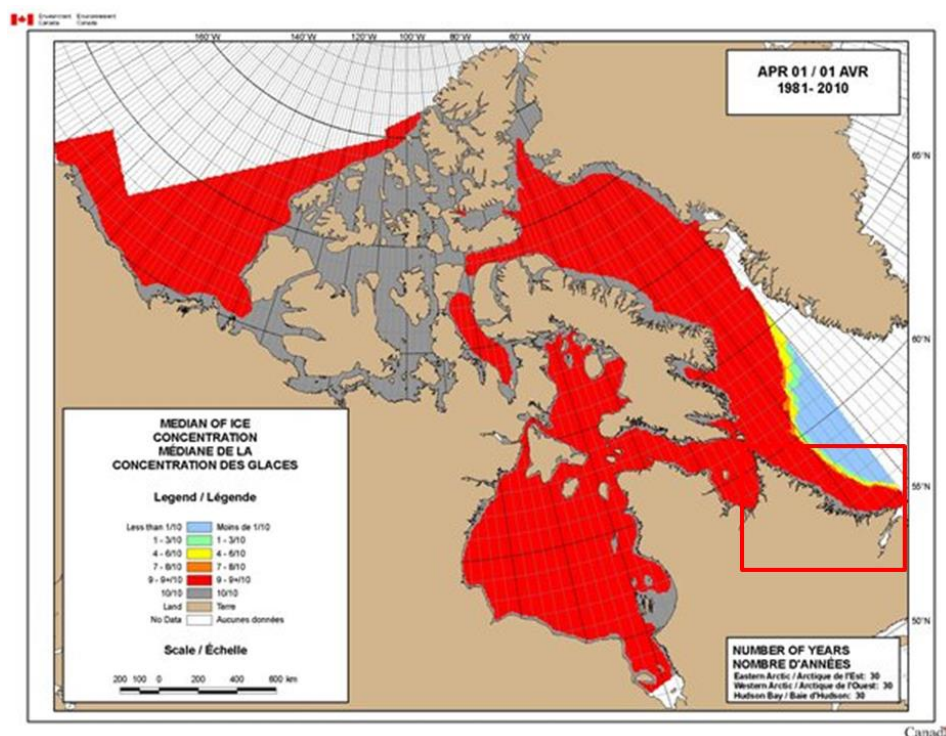


88 Coastal Labrador is dominated by the Labrador Current, which has a mean surface speed of $0.25\text{--}0.5\text{ m s}^{-1}$ (Lazier
 89 and Wright, 1993) toward the south and SSE, parallel to the coast (Figure 2).



90
 91 **Figure 2.** Mean surface currents offshore Labrador flow parallel to the coast toward the south and SSE at speeds of
 92 $0.25\text{--}0.5\text{ m s}^{-1}$ (image reproduced from Fenty and Heimbach, 2013).

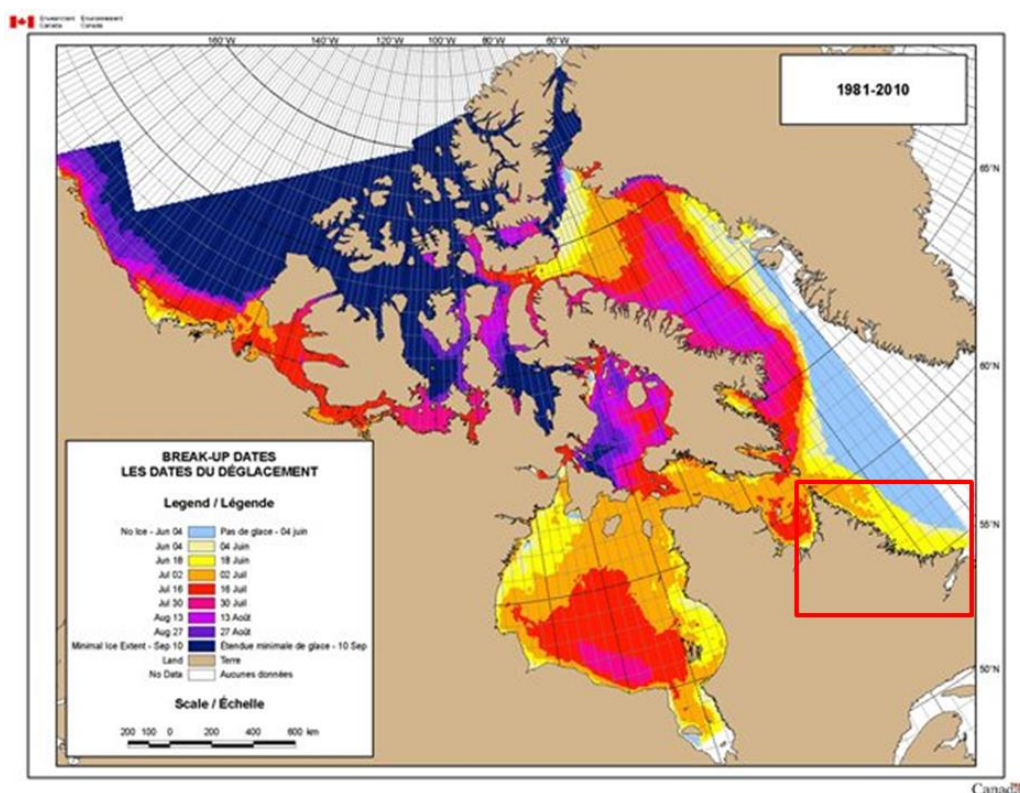
93 Freeze-up along the Labrador coast typically begins in December, with land-fast ice forming from the northern edge
 94 of Labrador to just south of Lake Melville (Canadian Coast Guard, 2013). By April 1st, a large region of 9+/10ths
 95 mainly first-year (FY) ice has formed further offshore from the land-fast ice and drifts southward with the Labrador
 96 Current, being replenished by more northerly-sourced ice from Baffin Bay (Figure 3). The boundary between the
 97 regions of 9+/10ths pack ice and open water is typically sharp and along the edge of the Labrador Shelf (see Figure
 98 5) near the western edge of the Labrador Current (Yao et al., 2000b), with only a thin band of ice 1-8/10ths in
 99 concentration along the boundary (Figure 3).



100

101 **Figure 3.** Maximum spring ice cover offshore Labrador (red-boxed region) typically includes a band of 10/10ths
 102 land-fast ice (gray region), and a more extensive zone of dynamic pack ice 9+/10ths in concentration (red region)
 103 further offshore (Canadian Coast Guard, 2013).

104 The onset of break-up of the high-concentration ice along the coast of Labrador typically occurs in mid-June for
 105 most of the region, with break-up commencing in early July for the most northerly areas (Figure 4).



106

107 **Figure 4.** The onset of pack ice break-up in the offshore Labrador region (red-boxed region) typically occurs in mid-
 108 June to early July (Canadian Coast Guard, 2013).

109 The water depth offshore Labrador extends to approximately 500 m along the Labrador Shelf, with a few pockets as
 110 deep as about 1000 m (Figure 5). Further offshore, the depth rapidly increases to greater than 2000 m. At its
 111 maximum seasonal extent in March-April, sea ice typically extends to the shelf break front (Yao et al., 2000b) along
 112 the 500 m depth contour.

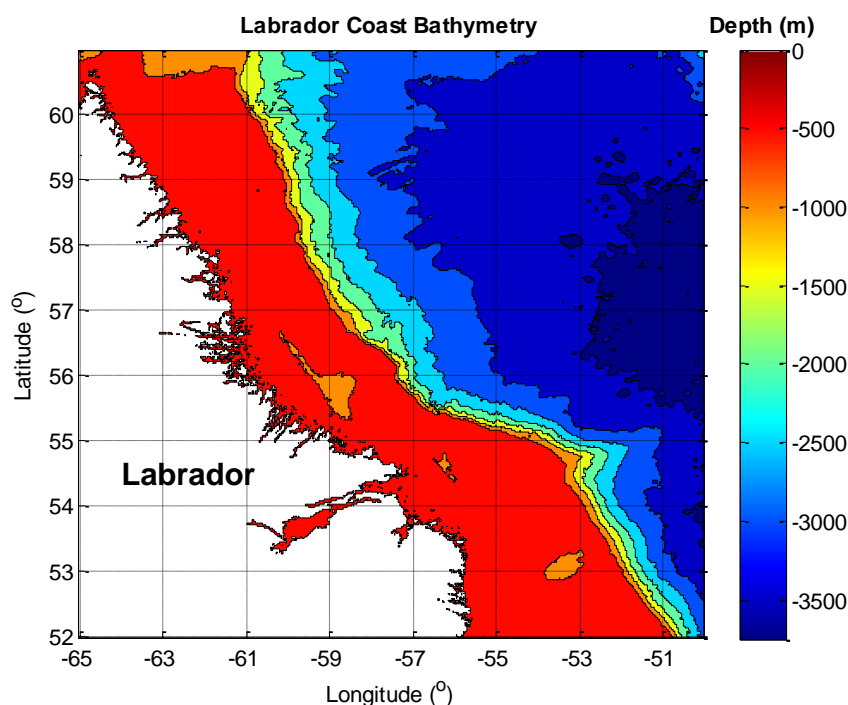


Figure 5. The bathymetry offshore Labrador (General Bathymetric Chart of the Oceans, GEBCO, 2008, 30-second data).

2 Ice Environmental Modeling

2.1 Previous modeling studies

Existing modelling studies for the offshore Labrador ice environment tend to focus on seasonal to inter-annual sea ice variability and its interaction with oceanic mixing and convection. Few studies have presented efforts to develop operational ice forecast models for the region.

A study by Peng, 1989, for example, applies a coupled ice-ocean model to simulate ice growth and transport in the Labrador Sea over a single winter season.

Prinsenbergh and Yao, 1999 presents a climatological study of the seasonal evolution of sea ice cover offshore eastern Canada for 1991-1992 using a three-dimensional coupled ice-ocean model. The study additionally presents model simulations of ice cover under a scenario of a doubling of atmospheric carbon dioxide concentration by using as input the expected atmospheric conditions under such a scenario.



127 A paper by Yao, 2000 focuses on the assimilation of satellite-derived sea surface temperature (SST) data into a
128 coupled ice-ocean model for the Labrador Sea, with the primary objective of improving the modelled location of the
129 ice edge. The SST data assimilation, however, did not improve model performance in this regard.

130 A study by Yao et al., 2000a focuses on verification of a coupled ice-ocean model for the Newfoundland shelf
131 during February-April 1997, with the region of interest (ROI) stretching from offshore central-northern
132 Newfoundland to southern Labrador. The model output was compared in particular to observed ice edge location,
133 southern ice extent, and ice thickness as derived from Canadian Ice Service (CIS) charts, and to ice drift velocities as
134 measured by satellite-tracked ice buoys.

135 Yao et al., 2000b presents results of a modelling study of the seasonal variation of sea ice in the Labrador Sea using
136 an ice model coupled to the Princeton ocean model. In this paper, the Princeton ocean model is forced by monthly
137 climatological atmospheric data.

138 A paper by Sayed et al., 2002 presents the operational ice dynamics model developed by CIS for ice forecasting in
139 regional environments. The model uses a Lagrangian Particle-In-Cell (PIC) approach to model ice advection. In the
140 paper, a seasonal simulation of the model is presented, with the ice model coupled to the Princeton ocean model.
141 The model output is compared with the measured trajectory of a single ice tracking beacon offshore Labrador during
142 January-April 1999, and with the January-May 1999 evolution of the total ice area and mean thickness over a large
143 area encompassing the east coast of Canada.

144 A study by Fenty and Heimbach, 2013 explores the relationship between sea ice and oceanic variability in the
145 Labrador Sea and Baffin Bay. It analyzes the response of the annual sea ice cover variability to ocean currents and
146 water mass mixing and convection in the region.

147 A paper by Cooke et al., 2014 presents a study of inter-annual sea ice variability in the western Labrador Sea using a
148 coupled sea ice-ocean model. The paper focuses on the relationships between sea ice concentration and the
149 underlying water column properties in terms of temperature, salinity, and convection. Cooke et al., 2014 use the
150 Nucleus for European Modelling of the Ocean (NEMO) model and couple it to the Louvain Sea Ice Model 2 (LIM2)
151 multi-layered sea ice model. Atmospheric forcing is provided by the National Center for Environmental
152 Prediction/National Center for Atmospheric Research (NCEP/NCAR) six-hourly reanalysis data from 1948-2005.

153 **2.2 Thermodynamic model description**

154 The model presented in this paper was developed in the programming language of MATLAB. The thermodynamic
155 model is largely based on the one-dimensional model presented in Ebert and Curry, 1993 (hereafter referred to as
156 EC93), which is in turn based on the model presented in Maykut and Untersteiner, 1971. The thermodynamic model
157 can be run as a standalone model, or can be coupled to the dynamic ice model. The thermodynamic model accounts
158 for heat fluxes from the surface ocean through the ice slab, heat exchanges with the surface air or snow layer if
159 present, snow layer accumulation, melt, and heat exchange with the ice and atmosphere, incoming shortwave (solar)
160 radiation, total cloud cover and its effects on atmospheric albedo and down-welling longwave radiation, and lead
161 and melt pond growth and contraction. The thermodynamic model-only runs are initialized with ice particles on a



grid with 0.45° spacing (approximately 50 km). Ice particles are dropped from the model grid once they have completely melted away.

2.2.1 Ice and snow thermal properties and heat conduction

In the thermodynamic model, the sea ice vertical temperature profile and thickness are governed by the one-dimensional heat equation as per EC93,

$$(\rho c)_i \left(\frac{\partial T_i}{\partial t} \right) = k_i \left(\frac{\partial^2 T_i}{\partial z^2} \right) = \frac{\partial F_c}{\partial z}, \quad (1)$$

where $(\rho c)_i$ is the volumetric heat capacity of ice, T_i is ice temperature (K), t is time (seconds), k_i is the thermal conductivity of ice, F_c is the upward conductive flux (W m^{-2}), and z is the depth level in the ice slab (m) with $z = 0$ defined at the ice surface. As the heat capacity and thermal conductivity of ice are affected by its temperature and salinity, the volumetric heat capacity of the sea ice ($\text{J m}^{-3} \text{K}^{-1}$) is defined as (*e.g.*, EC93),

$$(\rho c)_i = (\rho c)_{i,f} + \frac{\gamma S_i}{(T_i - 273)^2}, \quad (2)$$

where $(\rho c)_{i,f}$ is the volumetric heat capacity of pure ice ($1.883 \times 10^6 \text{ J m}^{-3} \text{K}^{-1}$) and γ is a constant ($1.715 \times 10^7 \text{ J K m}^{-3} \text{ppt}^{-1}$), and S_i is the ice salinity (ppt). The ice thermal conductivity ($\text{W m}^{-1} \text{K}^{-1}$) is defined as (*e.g.*, EC93),

$$k_i = k_{i,f} + \frac{BS_i}{T_i - 273}, \quad (3)$$

where $k_{i,f}$ is the thermal conductivity of pure ice ($2.034 \text{ W m}^{-1} \text{K}^{-1}$), and B is a constant ($0.1172 \text{ W m}^{-1} \text{ppt}^{-1}$). As per EC93, T_i is constrained to values 272.9K or less in order to avoid a singularity at 273K in Eqs. (2) and (3). The ice salinity (ppt) is approximated by the equation from Timco and Johnston, 2002 for cold FY ice as a function of thickness, *e.g.*,

$$\begin{aligned} S_i &= 13.4 - 17.4h_i & \text{for } h_i \leq 0.34\text{m}, \\ S_i &= 8.0 - 1.62h_i & \text{for } h_i > 0.34\text{m}, \end{aligned} \quad (4)$$

where h_i is ice thickness (m).

The ice temperature profile is initialized with a linear trend between the boundary conditions set at the ice base and surface. The ice basal temperature is fixed at the melting point of seawater, and the ice surface temperature is calculated as a function of the surface (2m) air temperature. The ice temperature is calculated at four evenly-spaced points in the vertical slab, including the boundaries at the ice-water and ice-snow or ice-air (when no snow is present) interfaces.

The snow-free ice surface temperature is calculated as a function of the surface air temperature according to the function (*e.g.*, Timco and Frederking, 1990),

$$\begin{aligned} T_{i,s} &= T_a & \text{for } -2 \geq T_a \geq -10, \\ T_{i,s} &= 0.6T_a - 4 & \text{for } T_a < -10, \end{aligned}$$



$$T_{i,s} = -2.0 \quad \text{for } T_a > -2, \quad (5)$$

where $T_{i,s}$ is the ice surface temperature ($^{\circ}\text{C}$), and T_a is the 2 m air temperature ($^{\circ}\text{C}$). When the air temperature is higher than -2°C , the ice surface temperature is assumed to be at the approximate freezing point of saline FY sea ice, -2°C .

The basal ice temperature is calculated as the freezing temperature of seawater as a function of sea surface salinity (*e.g.*, Fofonoff and Millard Jr., 1983),

$$T_{o,f} = -5.33 \times 10^{-7} S^3 - 9.37 \times 10^{-6} S^2 - 0.0592 S, \quad (6)$$

where $T_{o,f}$ is the freezing temperature of seawater ($^{\circ}\text{C}$), and S is the sea surface salinity (ppt).

When a snow layer is present on the sea ice, the snow vertical temperature profile is governed by a similar one-dimensional heat equation as that used for sea ice (*e.g.*, EC93),

$$(\rho c)_s \left(\frac{\partial T_s}{\partial t} \right) = k_s \left(\frac{\partial^2 T_s}{\partial z^2} \right) = \frac{\partial F_c}{\partial z}, \quad (7)$$

where $(\rho c)_s$ is the volumetric heat capacity of snow, T_s is the snow temperature (K), k_s is the thermal conductivity of snow, and z is again defined with $z = 0$ at the snow surface. The snow temperature is calculated at three evenly-spaced points in the vertical slab, including the boundaries at the snow-ice and snow-air interfaces. The volumetric heat capacity of snow is given by (*e.g.*, EC93),

$$(\rho c)_s = \rho_s (92.88 + 7.364 T_s), \quad (8)$$

where ρ_s is the density of the snow layer (kg m^{-3}) on the sea ice. The value of ρ_s is 330 kg m^{-3} if the surface air temperature is less than 0°C , and is 450 kg m^{-3} if the surface air temperature is 0°C or greater (EC93). Compaction of the snow layer due to fresh snowfall and time is neglected in the present model. The snow thermal conductivity is given by (*e.g.*, EC93),

$$k_s = 2.845 \times 10^{-6} \rho_s^2 + 2.7 \times 10^{-4} \times 2^{\frac{T_s - 233}{5}}. \quad (9)$$

The temperature at the snow-ice interface is computed from Eq. (7) and is set to the ice surface temperature. The temperature at the snow-air interface is initialized in K by (*e.g.*, Tonboe et al., 2011),

$$\begin{aligned} T_{s,top} &= 1.14 T_a - 37.94 & \text{for } T_a < 273.15, \\ T_{s,top} &= 273.15 & \text{for } T_a \geq 273.15. \end{aligned} \quad (10)$$

Snow temperatures are constrained to 0°C and below. The effect of sea water flooding on the snow surface is neglected in this model. As with the vertical ice temperature profiles, at the start of each model run, the vertical snow temperatures are initialized with linear vertical profiles. From the second time-step forward, the temperature at the snow or snow-free ice surface is solved using the net surface heat flux (see Eq. 49 in section 2.2.7).

2.2.2 Solar radiation



222 The incoming solar (shortwave) radiation (W m^{-2}) at the top of the atmosphere is given by (e.g., FAO, 2015),

$$223 F_{SW} = \frac{12S_0 d_r ((\omega_2 - \omega_1) \sin(\phi) \sin(\lambda) + \cos(\phi) \cos(\lambda) (\sin(\omega_2) - \sin(\omega_1)))}{\pi}, \quad (11)$$

224 where S_0 is the solar constant (1365.5 W m^{-2}), d_r is the inverse relative Earth-Sun distance (radians), ω_1 and ω_2 are
 225 the solar time angles (radians) immediately before and after a given time-step, respectively, ϕ is the latitude
 226 (radians), and λ is the solar declination (radians). The inverse relative Earth-Sun distance is defined by (e.g., FAO,
 227 2015),

$$228 d_r = 1 + 0.033 \cos\left(\frac{2\pi J}{365}\right), \quad (12)$$

229 where J is the Julian date. The solar declination is defined by (e.g., FAO, 2015),

$$230 \lambda = 0.409 \sin\left(\frac{2\pi J}{365} - 1.39\right). \quad (13)$$

231 The solar time angles are given by (e.g., FAO, 2015),

$$232 \omega_1 = \omega - \frac{\pi dt}{24},$$

$$233 \omega_2 = \omega + \frac{\pi dt}{24}, \quad (14)$$

234 where ω is the solar time angle (radians) at the midpoint of the period over which the incoming solar radiation is
 235 calculated, and dt is the length of the calculation period (hours). The solar time angle at the midpoint of the period is
 236 defined by (e.g., FAO, 2015),

$$237 \omega = \frac{\pi((t + 0.06667(L_z - L_m) + S_c) - 12)}{12}, \quad (15)$$

238 where t is the standard clock time at the hour midpoint (e.g., $t = 13.5$ if the calculation time is between 13:00 and
 239 14:00 hours), L_z is the longitude of the center of the local time zone (60°W for the Atlantic Standard Time or AST
 240 zone) in degrees west of Greenwich, L_m is the longitude of the calculation site in degrees west of Greenwich, and S_c
 241 is the seasonal correction for solar time (hours). The solar time seasonal correction is given by (e.g., FAO, 2015),

$$242 S_c = 0.1645 \sin(2b) - 0.1255 \cos(b) - 0.025 \sin(b), \quad (16)$$

243 where b is defined as $\frac{2\pi(J-81)}{364}$ (FAO, 2015).

244 Finally, the sunset hour angle ω_s (radians) is used to determine whether or not the sun is below the horizon at a
 245 given time. The sunset hour angle is defined as (e.g., FAO, 2015),

$$246 \omega_s = \arccos(-\tan(\phi) \tan(\lambda)). \quad (17)$$

247 The sun is below the horizon when $\omega < -\omega_s$ or $\omega > \omega_s$ and $F_{SW} = 0$. Note that times used to calculate F_{SW} are
 248 local times for AST, which is UTC-3:00 during April-May.

249 The flux of solar radiation (W m^{-2}) which penetrates the snow-free ice surface as a function of depth in the ice, z
 250 (m), is governed by Beer's Law (e.g., EC93),



$$F_{i0}(z) = I_0(1 - \alpha_i)F_{SW}e^{-\kappa_i(z)}, \quad (18)$$

where I_0 is the fraction of solar radiation which penetrates the atmosphere, α_i is the ice albedo, and κ_i is the bulk shortwave extinction coefficient for sea ice (1.5 m^{-1}). The fraction of solar radiation penetrating the atmosphere is defined by (e.g., EC93),

$$I_0 = 0.18(1 - T_{cc}) + 0.35T_{cc}, \quad (19)$$

where T_{cc} is the total fractional cloud cover. If there is snow on the sea ice, then Eq. (18) becomes,

$$F_{i0}(z) = (1 - \alpha_i)F_{i0,s}e^{-\kappa_i(z)}, \quad (20)$$

where $F_{i0,s}$ is the fraction of solar radiation which penetrates the snow layer. The fraction of solar radiation penetrating the snow layer is given by,

$$F_{i0,s} = I_0(1 - \alpha_s)F_{SW}e^{-\kappa_s(z)}, \quad (21)$$

where α_s is the snow albedo, κ_s is the bulk shortwave extinction coefficient for snow (0.42 m^{-1} as per Davis, 1996), and z (m) is the depth in the snow layer. The fractions of penetrating solar radiation determined from Eqs. (18) and (21) are used to update the ice and snow temperature profiles as computed from Eqs. (1) and (7), respectively. In Eqs. (1) and (7), the quantity F_c is replaced with F_{i0} and $F_{i0,s}$, respectively.

2.2.3 Meltwater ponds

The model presented here allows for the growth and contraction of meltwater ponds on the surface of the sea ice in terms of the depth and fractional area coverage of the ponds. The rate of meltwater pond depth change (m s^{-1}) is defined by (e.g., EC93 and Holland et al., 2012),

$$\frac{\partial h_p}{\partial t} = \left((1 - A_{pond}) \left(\frac{\partial h_i}{\partial t} \right)_0 + \frac{A_{pond}F_p}{L_{fi}} + RF + \frac{SF\rho_s}{\rho_w} \right) (1 - r), \quad (22)$$

where h_p is pond depth (m), A_{pond} is pond fractional area, $\left(\frac{\partial h_i}{\partial t} \right)_0$ is the rate of ice melt at the top surface of the sea ice (m s^{-1}), F_p is the solar radiation flux (W m^{-2}) which is absorbed by both the pond water and the underlying sea ice, L_{fi} is the latent heat of fusion of sea ice ($3.014 \times 10^8 \text{ J m}^{-3}$), RF and SF are rainfall and snowfall, respectively (m s^{-1}), ρ_w is the density of melt-pond water (1000 kg m^{-3}), and r is the fraction of surface meltwater and rainfall which runs off the ice surface while the rest remains in the ponds. The quantity r is defined as $0.85 - 0.7A_{ice}$ (Holland et al., 2012), where A_{ice} is the fractional ice area concentration of a given model particle. As per EC93, once the melt-pond depth on a given model particle is greater than zero, the melt-pond fractional area is initialized at 0.10.

The flux of solar radiation absorbed by the pond water and sea ice is defined by (e.g., EC93),

$$F_p = F_{SW} \left(a_p + a_p\alpha_i t_p + t_p(1 - \alpha_i)(1 - I_0) \right) (1 - \alpha_p), \quad (23)$$



where a_p is the pond absorption coefficient ($1 - t_p^{0.89}$), t_p is the pond transmissivity ($0.36 - 0.17 \log_{10}(h_p)$), and α_p is the pond albedo. As per EC93, the maximum allowed melt-pond depth is set to 0.8 m. Any melt-ponds which grow to a depth greater than the ice thickness (when the ice thickness is less than 0.8 m) are subsequently treated as leads in the ice pack (see subsection 2.2.4).

One melt ponds have begun to form, the melt-pond fractional area is computed iteratively using the scheme of Holland et al., 2012 which allows for growth and contraction of the ponds based on the ice surface temperature. The evolution of the melt-pond fractional area in terms of growth and contraction is defined respectively as follows,

$$A_{pond(i+1)} = A_{pond(i)} + \frac{(1-r) \left(\left(\frac{\partial h_i}{\partial t} \right)_0 \left(\frac{\rho_i}{\rho_w} \right) + RF \right)}{h_p} dt \quad \text{for } T_{i,s} > -2^\circ\text{C},$$

$$A_{pond(i+1)} = A_{pond(i)} e^{\frac{0.01(T_{i,s}+2)}{2}} \quad \text{for } T_{i,s} \leq -2^\circ\text{C}, \quad (24)$$

where i is the model time-step index, and dt is the model time-step (seconds). As per EC93, the melt-pond fractional area is restricted to a maximum value of 0.25. Melt-ponds are not permitted to form until all of the snow has melted from a model particle.

2.2.4 Lead development and ocean heat fluxes

The present model uses the parameterizations of EC93 to simulate the ocean-air and ocean-ice heat exchanges and the development of leads in the ice pack. The net heat flux (W m^{-2}) at the lead surface is defined by (e.g., EC93),

$$F_{lead} = \epsilon_w F_{LW} - \epsilon_w \sigma T_w^4 + (1 - \alpha_w)(1 - i_w) F_{SW} - F_{sens,w} - F_{lat,w}, \quad (25)$$

where ϵ_w is the emissivity of water (0.97), F_{LW} is the incoming (downward) infrared heat flux from the atmosphere (W m^{-2}), σ is the Stefan-Boltzmann constant ($5.67 \times 10^{-8} \text{ W m}^{-2} \text{ K}^{-4}$), T_w is the surface ocean temperature (K), α_w is the surface ocean albedo, i_w is the fraction of solar radiation transmitted through the surface water layer equivalent in depth to the ice thickness and not absorbed, and $F_{sens,w}$ and $F_{lat,w}$ are the sensible and latent heat fluxes from the ocean surface layer, respectively (W m^{-2}). The parameter i_w is defined as follows (e.g., EC93),

$$i_w = 1 - \frac{(a_1 + a_2 \ln(h_i))}{1 - \alpha_w}, \quad (26)$$

where $a_1 = 0.5676$ and $a_2 = 0.1046$ under clear-sky conditions and $a_1 = 0.3938$ and $a_2 = 0.1208$ under cloudy-sky conditions. In the present model, conditions are considered to be clear-sky if the total cloud area fraction is less than 0.35.

The growth of the fractional lead area is defined by (e.g., EC93),

$$\frac{\partial A_{lead}}{\partial t} = \frac{A_{lead} F_{lead}}{L_{fi} h_i + L_{fs} h_s}, \quad (27)$$

where L_{fs} is the latent heat of fusion of snow ($1.097 \times 10^8 \text{ J m}^{-3}$), and h_s is the thickness of the snow layer on the ice (m).



308 The expression for the solar radiation flux (W m^{-2}) absorbed beneath the ice is represented as the sum of the solar
 309 flux through the leads and the solar radiation transmitted through snow-free ice and is given as follows (*e.g.*, EC93),

$$310 F_{wi} = A_{lead}(1 - \alpha_w)i_w F_{SW} + (1 - A_{lead})(1 - \alpha_i)I_0 e^{-\kappa_i h_i} F_{SW}. \quad (28)$$

311 The water temperature immediately beneath the ice, T_{wi} , is governed by (*e.g.*, EC93),

$$312 \frac{\partial T_{wi}}{\partial t} = \frac{F_{wi} - (1 - A_{lead})F_b}{(d_w - (\frac{\rho_i}{\rho_w})h_i)(\rho c)_w}, \quad (29)$$

313 where F_b is the heat flux at the base of the ice (W m^{-2}), d_w is the ocean mixed layer depth (m), and $(\rho c)_w$ is the
 314 volumetric heat capacity of water ($4.19 \times 10^6 \text{ J m}^{-3} \text{ K}^{-1}$). In deeper water, the ocean mixed layer depth is assumed to
 315 be 30 m (EC93), and is assumed to be the bathymetric water depth in shallower water less than 30 m deep (see
 316 Figure 5). The model is initialized with $T_{wi} = T_{o,f}$ as per Eq. (6). The heat flux at the base of the ice is given by
 317 (*e.g.*, EC93),

$$318 F_b = (\rho c)_w C_{Tb} (T_{wi} - T_{o,f}), \quad (30)$$

319 where C_{Tb} is the bulk transfer coefficient. As per EC93, C_{Tb} is defined as,

$$320 C_{Tb} = 1.26 \times 10^{-4} h_i^{-0.5} \quad \text{for } h_i < 3 \text{ m},$$

$$321 C_{Tb} = 7.27 \times 10^{-5} \quad \text{for } h_i \geq 3 \text{ m}. \quad (31)$$

322 2.2.5 Atmospheric properties and heat fluxes

323 The ocean and ice atmospheric heat fluxes in the present model are defined by the bulk aerodynamic formulae for
 324 sensible, latent, and longwave radiative heat transfer as per EC93. The sensible heat flux over ice (W m^{-2}) is defined
 325 as (*e.g.*, EC93),

$$326 F_{sens,i} = \rho_a c_{pa} C_{Ti} U_a (T_{i,s} - T_a), \quad (32)$$

327 where ρ_a is the air density (kg m^{-3}) at 2 m, c_{pa} is the specific heat of air at constant pressure ($\text{J kg}^{-1} \text{ K}^{-1}$), C_{Ti} is the
 328 bulk heat and moisture transfer coefficient over ice, and U_a is the wind speed at 2 m (m s^{-1}). The air density is
 329 computed according to the ideal gas law as (*e.g.*, Tsonis, 2002),

$$330 \rho_a = \frac{P_s}{RT_a}, \quad (33)$$

331 where P_s is the surface or sea level atmospheric pressure (Pa), R is the gas constant for air ($\text{J kg}^{-1} \text{ K}^{-1}$), and the 2 m
 332 air temperature T_a is in K. The gas constant for air depends on the air specific humidity as follows (*e.g.*, Tsonis,
 333 2002),

$$334 R = R_d(1 + 0.61q_a), \quad (34)$$

335 where R_d is the gas constant for dry air ($278.058 \text{ J kg}^{-1} \text{ K}^{-1}$), and q_a is the specific humidity of the air at 2 m. The air
 336 specific humidity is defined by (*e.g.*, Tsonis, 2002),



$$q_a = \frac{\frac{0.622e_w}{p_s - e_w}}{1 + \left(\frac{0.622e_w}{p_s - e_w}\right)}, \quad (35)$$

where e_w is the vapor pressure in the air (Pa) at 2 m. The vapor pressure is equivalent to $(RH)(e_{sw})$, where RH is the relative humidity at 2 m, and e_{sw} is the saturation vapor pressure (Pa) at 2 m. The saturation vapor pressure is given by (e.g., Tsonis, 2002),

$$e_{sw} = 611e^{19.83 - \frac{5417}{T_a}}, \quad (36)$$

where T_a is in K. The specific heat of air at constant pressure is defined as $\frac{7}{2}R$ (Tsonis, 2002). The bulk heat and moisture transfer coefficient over ice is defined as (e.g., EC93),

$$C_{Ti} = C_{T0i} \left(1 - \frac{2b_a Ri_{ice}}{1 + c |Ri_{ice}|^{0.5}}\right) \quad \text{for } Ri_{ice} < 0, \\ C_{Ti} = C_{T0i} (1 + b_a Ri_{ice})^{-2} \quad \text{for } Ri_{ice} \geq 0, \quad (37)$$

where C_{T0i} is a heat and moisture transfer coefficient for a neutral surface layer over ice (1.3×10^{-3}), b_a is a parameter for atmospheric turbulence equal to 20, Ri_{ice} is the bulk Richardson number over ice, and c has a value of $(1961b_a C_{T0i})$ for an ice roughness length of 1.6×10^{-4} m. The Richardson number is defined as (e.g., EC93),

$$Ri_{ice} = \frac{g(T_a - T_{is})\Delta z}{T_a u_a^2}, \quad (38)$$

where g is the earth gravitational acceleration (9.81 m s^{-2}), and Δz is the height of the wind speed and air temperature data (2 m).

The latent heat flux over sea ice (W m^{-2}) is given as (e.g., EC93),

$$F_{lat,i} = \rho_a L_v C_{Ti} U_a (q_{sat}(T_{i,s}) - q_a), \quad (39)$$

where L_v is the latent heat of vaporization ($2.501 \times 10^6 \text{ J m}^{-3}$), and $q_{sat}(T_{i,s})$ is the saturation specific humidity over ice. This quantity is equal to (e.g., WHOI, 2010),

$$q_{sat}(T_{i,s}) = \frac{0.622e_{sat,i}}{p_s - 0.378e_{sat,i}}, \quad (40)$$

where $e_{sat,i}$ is the saturation vapor pressure directly over the ice (Pa), which is equivalent to (e.g., WHOI, 2010),

$$e_{sat,i} = 10^{\frac{0.7859 + 0.03477T_{i,s} + 0.00422T_{i,s}^2}{1 + 0.00412T_{i,s}}}. \quad (41)$$

As per EC93, the formulas for the sensible and latent heat fluxes over leads and open water (W m^{-2}), $F_{sens,w}$ and $F_{lat,w}$, respectively, are similar to those for ice (Eqs. 32 and 39). For the sensible heat flux over water, the quantity $T_{i,s}$ in Eq. (32) is replaced with T_w to represent the surface water temperature. In Eq. (32), the bulk heat and moisture transfer coefficient over water, C_{Tw} , is determined using Equation 37 with $C_{T0} = 1.0 \times 10^{-3}$ over water, and the bulk Richardson number over water, Ri_{water} , is calculated by replacing T_a with T_w in Eq. (38). The latent heat flux over water is computed by replacing C_{Ti} with C_{Tw} in Equation 39, and $q_{sat}(T_{i,s})$ with $q_{sat}(T_w)$, the saturation specific



humidity over water. The quantity is computed from Equation 40, however saturation vapor pressure directly over water, $e_{sat,w}$ (Pa), is determined by replacing $T_{i,s}$ with T_w in Equation 41, and multiplying Eq. (41) by 0.98.

The downward longwave (infrared) radiative flux from the atmosphere to the ocean and ice (Wm^{-2}) is defined by (e.g., König-Langlo and Augstein, 1994),

$$F_{LW} = (0.765 + 0.22T_{cc}^3)\sigma T_a^4, \quad (42)$$

where the quantity $(0.765 + 0.22T_{cc}^3)$ represents the atmospheric emissivity as a function of the total fractional cloud cover area.

2.2.6 Albedo

The surface albedo parameterization follows the scheme used in EC93, in which there are five surface types considered: dry snow, melting snow, bare ice, meltwater ponds, and open water. The albedo scheme additionally considers the spectral variation in the incoming shortwave radiation in four ranges of wavelength, as well as the albedo dependence on solar zenith angle. The solar zenith angle is given by,

$$\theta_0 = \arccos(\mu_0), \quad (43)$$

where the quantity μ_0 is defined as,

$$\mu_0 = \sin(\phi) \sin(\delta) + \cos(\phi) \cos(\delta) \cos(\theta_h). \quad (44)$$

In Eq. (44), δ is defined as (e.g., NOAA, 2015),

$$\delta = 0.006918 - 0.399912 \cos(d) + 0.070257 \sin(d) - 0.006758 \cos(2d) + 0.000907 \sin(2d) - 0.002697 \cos(3d) + 0.00148 \sin(3d), \quad (45)$$

where the quantity d is defined by $d = \frac{2\pi(J-1)}{365.2422}$ and is given in radians. In Eq. (44), θ_h is the hour angle, and is defined as $\theta_h = 15(T_{hr} - M) - L_m$, in which T_{hr} is the hour of the day (e.g., 13 for 13:00) and M is defined by (e.g., NCEP, 2015),

$$M = 12 + 0.12357 \sin(d) - 0.004289 \cos(d) + 0.153809 \sin(2d) + 0.060783 \cos(2d). \quad (46)$$

The relative weights assigned to each wavelength band of the solar spectrum, as well as the fractions of diffuse versus direct radiation, are summarized in Table 2 as a function of month (e.g., EC93).

Table 2. Summary of solar spectrum relative weights as a function of wavelength band and month, as well as fractions of diffuse versus direct radiation (EC93).

Solar Spectrum Weights and Radiation Fractions for Surface Albedo						
Month	Wavelength Band (μm)				Diff. Rad. (DR) Fraction	Direct Rad. (1 – DR) Fraction
	0.25 - 0.69	0.69 - 1.19	1.19 - 2.38	2.38 - 4.00		
Jan	0.520	0.343	0.129	0.008	0.779	0.221



Feb	0.520	0.343	0.129	0.008	0.779	0.221
Mar	0.503	0.343	0.142	0.012	0.658	0.342
Apr	0.492	0.339	0.153	0.016	0.489	0.511
May	0.504	0.338	0.144	0.014	0.581	0.419
Jun	0.527	0.340	0.124	0.009	0.724	0.276
Jul	0.545	0.315	0.130	0.010	0.698	0.302
Aug	0.539	0.321	0.130	0.010	0.715	0.285
Sep	0.517	0.339	0.134	0.010	0.717	0.283
Oct	0.519	0.343	0.130	0.008	0.790	0.210
Nov	0.520	0.343	0.129	0.008	0.779	0.221
Dec	0.520	0.343	0.129	0.008	0.779	0.221

391 The albedo is then given as (e.g., EC93),

$$392 \quad \alpha = (DR)(\sum_{j=1}^4 w_j \alpha_{j(DR)}) + (1 - DR)(\sum_{j=1}^4 w_j \alpha_{j(1-DR)}), \quad (47)$$

393 where w_j is the weight of a given wavelength band, α_j is the albedo in that band, DR refers to the fraction of diffuse
 394 radiation, and $(1 - DR)$ refers to the fraction of direct radiation. Table 3 summarizes the albedo values as functions
 395 of the wavelength band of the incoming shortwave radiation spectrum, the surface type, direct or diffuse radiation,
 396 and ice and snow thickness, and is reproduced here from Table 2 in EC93.

397 **Table 3.** Spectral albedos for the various surface types, reproduced here from Table 2 in EC93.

Spectral Albedos for Five Surface Types				
Surface Type	Wavelength Band (μm)			
	0.25 - 0.69	0.69 - 1.19	1.19 - 2.38	2.38 - 4.00
Dry snow, α_s				
Direct Rad.	$0.980 - 0.008\mu_0$	$0.902 - 0.116\mu_0$	$0.384 - 0.222\mu_0$	$0.053 - 0.047\mu_0$
Diffuse Rad.	0.975	0.832	0.250	0.025
Melting snow, α_s				
$h_s \geq 0.1\text{m}$	0.871	0.702	0.079	0.010
$h_s < 0.1\text{m}$	linearly reduced to bare sea ice value	linearly reduced to bare sea ice value	linearly reduced to bare sea ice value	linearly reduced to bare sea ice value



				value
Bare sea ice, α_i				
$h_i < 1\text{m}$	$0.760 + 0.140\ln(h_i)$	$0.247 + 0.029\ln(h_i)$	0.055	0.036
$1\text{m} \leq h_i < 2\text{m}$	$0.770 + 0.018(h_i - 1)$	$0.247 + 0.196(h_i - 1)$	0.055	0.036
$h_i \geq 2\text{m}$	0.778	0.443	0.055	0.036
Meltwater pond, α_p	$0.150 + \exp(-8.1h_p - 0.47)$	$0.054 + \exp(-31.8h_p - 0.94)$	$0.033 + \exp(-2.6h_p - 3.82)$	0.030
Open water/leads, α_w				
Direct Rad.	$\alpha_w^* + 0.008$	$\alpha_w^* - 0.007$	$\alpha_w^* - 0.007$	$\alpha_w^* - 0.007$
Diffuse Rad.	0.060	0.060	0.060	0.060

398 In Table 3, h_s is snow depth (m), and the value α_w^* is defined as (e.g., EC93),

$$399 \quad \alpha_w^* = \frac{0.026}{\mu_0^{1.7} + 0.065} + 0.015(\mu_0 - 0.1)(\mu_0 - 0.5)(\mu_0 - 1.0). \quad (48)$$

400 2.2.7 Energy balance and thickness changes over snow and ice

401 The energy balance at the surface of the snow or snow-free ice layer is represented by (e.g., EC93),

$$402 \quad (F_{net})_0 = \epsilon(F_{LW} - \sigma T_0^4) + (1 - \alpha)(1 - I_0)F_{SW} - F_{sens} - F_{lat} = -(F_c)_0, \quad (49)$$

403 where ϵ is the emissivity of the snow or ice (0.99), T_0 is the temperature of the snow or ice surface (K), α is the
 404 snow or ice albedo, and $(F_c)_0$ is the conductive heat flux at the snow or ice surface (W m^{-2}). Eq. (49) is used to solve
 405 for the snow or snow-free ice surface temperature after the first time-step.

406 Changes in snow and ice thickness are governed by the energy balances at the snow and ice surfaces and the base of
 407 the ice, and the volumetric heats of fusion for snow and ice. The rate of change in snow thickness at the surface is
 408 given by (e.g., EC93),

$$409 \quad \left(\frac{\partial h_s}{\partial t}\right)_0 = \frac{-F_{net} - (F_c)_0}{L_{fs}}, \quad (50)$$

410 where L_{fs} is the volumetric heat of fusion for snow ($1.097 \times 10^8 \text{ J m}^{-3}$). Similarly, the rate of change in thickness at
 411 the surface of the snow-free ice is given by (e.g., EC93),

$$412 \quad \left(\frac{\partial h_i}{\partial t}\right)_0 = \frac{-F_{net} - (F_c)_0}{L_{fi}}, \quad (51)$$

413 where L_{fi} is the volumetric heat of fusion for ice ($3.014 \times 10^8 \text{ J m}^{-3}$). Changes in thickness at the ice surface are
 414 constrained to be $\left(\frac{\partial h_i}{\partial t}\right)_0 \leq 0$ so that ice growth only occurs through accretion at the base. The accretion or melting
 415 at the base of the ice is defined by (e.g., EC93),



$$\left(\frac{\partial h_i}{\partial t}\right)_b = \frac{(F_c)_b - F_b}{L_{fb}}, \quad (52)$$

where $(F_c)_b$ is the conductive heat flux at the base of the ice (W m^{-2}), and L_{fb} is the volumetric heat of fusion for ice at the base ($2.679 \times 10^8 \text{ J m}^{-3}$).

2.3 Dynamic model description

The dynamic model is based on the Smoothed Particle Hydrodynamics (SPH) formulation as originally applied to ice dynamics in Gutfraind and Savage, 1997 and Lindsay and Stern, 2004. The dynamic model is coupled to the thermodynamic model, and is run at each time-step immediately after the thermodynamic model. It is forced by surface wind speed and direction, surface current speed and direction, Coriolis deflection, the horizontal gradient of the sea surface slope, internal ice stresses, and a coastal boundary force. As per Lindsay and Stern, 2004, particles which drift within 0.4 of the initial grid spacing are combined into a single particle.

2.3.1 Air drag

The zonal and meridional components of the acceleration (m s^{-2}) on each Lagrangian ice particle due to wind forcing are given by,

$$\begin{aligned} \overrightarrow{A_{wx}} &= \left(\frac{1}{\rho_i h_i}\right) \rho_a C_a \sqrt{(\overrightarrow{u_a} - \overrightarrow{u_i})^2 + (\overrightarrow{v_a} - \overrightarrow{v_i})^2} (\overrightarrow{u_a} - \overrightarrow{u_i}), \\ \overrightarrow{A_{wy}} &= \left(\frac{1}{\rho_i h_i}\right) \rho_a C_a \sqrt{(\overrightarrow{u_a} - \overrightarrow{u_i})^2 + (\overrightarrow{v_a} - \overrightarrow{v_i})^2} (\overrightarrow{v_a} - \overrightarrow{v_i}), \end{aligned} \quad (53)$$

respectively, where C_a is the dimensionless air drag coefficient (2.0×10^{-3}), $\overrightarrow{u_a}$ and $\overrightarrow{u_i}$ are the zonal velocities for wind and ice drift, respectively, and $\overrightarrow{v_a}$ and $\overrightarrow{v_i}$ are the meridional velocities for wind and ice drift, respectively (m s^{-1}).

2.3.2 Water drag

The zonal and meridional components of the acceleration (m s^{-2}) on the ice particles due to ocean current forcing are similar to those for the wind and are given by,

$$\begin{aligned} \overrightarrow{A_{ox}} &= \left(\frac{1}{\rho_i h_i}\right) \rho_{wo} C_w \sqrt{(\overrightarrow{u_w} - \overrightarrow{u_i})^2 + (\overrightarrow{v_w} - \overrightarrow{v_i})^2} (\overrightarrow{u_w} - \overrightarrow{u_i}), \\ \overrightarrow{A_{oy}} &= \left(\frac{1}{\rho_i h_i}\right) \rho_{wo} C_w \sqrt{(\overrightarrow{u_w} - \overrightarrow{u_i})^2 + (\overrightarrow{v_w} - \overrightarrow{v_i})^2} (\overrightarrow{v_w} - \overrightarrow{v_i}), \end{aligned} \quad (54)$$

respectively, where ρ_{wo} is the density of seawater (kg m^{-3}), C_w is the dimensionless water drag coefficient (5.0×10^{-3}), and $\overrightarrow{u_w}$ and $\overrightarrow{v_w}$ are the zonal and meridional velocities for the surface current, respectively (m s^{-1}). The density of seawater is computed by (e.g., Fofonoff and Millard Jr., 1983),

$$\begin{aligned} \rho_{wo} &= 999.842594 + 6.793952 \times 10^{-2} T_w - 9.09529 \times 10^{-3} T_w^2 + 1.001685 \times 10^{-4} T_w^3 - 1.120083 \times \\ &10^{-6} T_w^4 + 6.536332 \times 10^{-9} T_w^5 + (8.24493 \times 10^{-1} - 4.0899 \times 10^{-3} T_w + 7.6438 \times 10^{-5} T_w^2 - 8.2467 \times \end{aligned}$$



$$10^{-7}T_w^3 + 5.3875 \times 10^{-9}T_w^4)S + (-5.72466 \times 10^{-3} + 1.0227 \times 10^{-4}T_w - 1.6546 \times 10^{-6}T_w^2)S^{1.5} + 4.8314 \times 10^{-4}S^2, \quad (55)$$

where T_w is the SST ($^{\circ}\text{C}$).

2.3.3 Coriolis deflection

The zonal and meridional components of the acceleration (m s^{-2}) on the ice particles due to Coriolis forcing are given by,

$$\begin{aligned} \vec{A}_{cx} &= f\vec{v}_t, \\ \vec{A}_{cy} &= -f\vec{u}_t, \end{aligned} \quad (56)$$

respectively. In Eq. (56), f is the Coriolis parameter (s^{-1}) and is defined by $2\omega_e \sin(\phi)$, where ω_e is the Earth angular speed ($7.292115 \times 10^{-5} \text{ rad s}^{-1}$).

2.3.4. Sea surface gradient forcing

The zonal and meridional components of the horizontal gravitational acceleration (m s^{-2}) on the ice particles due to the sea surface gradient are given by,

$$\begin{aligned} \vec{A}_{gx} &= -g\nabla H_x, \\ \vec{A}_{gy} &= -g\nabla H_y, \end{aligned} \quad (57)$$

respectively, where ∇H_x and ∇H_y are the zonal and meridional gradients of the sea surface.

2.3.5. Internal ice stresses

The first step in calculating the internal ice stresses is to project the ice particle positions from their latitude-longitude grid onto a Cartesian grid in order to facilitate computations of distance between the particles. The northing-easting grid chosen for this work is the Mercator projection. Conversions of latitude and longitude to Mercator northing, y , and easting, x , coordinates (m) are defined by,

$$\begin{aligned} y &= R_e k \ln \left(\tan \left(\frac{\pi}{4} + \frac{\phi}{2} \right) \right), \\ x &= R_e k L, \end{aligned} \quad (58)$$

respectively, where R_e is the radius of the earth ($6371 \times 10^3 \text{ m}$), k is the scale factor for 55°N latitude (1.75), and L is the longitude (radians).

The zonal and meridional components of the acceleration (m s^{-2}) on the ice particles due to internal stress gradients are given by (e.g., Lindsay and Stern, 2004),

$$\vec{A}_{sx} = \left(\frac{1}{\rho_i h_i} \right) \left(\frac{\partial \sigma_{xx}}{\partial x} + \frac{\partial \sigma_{xy}}{\partial y} \right),$$



$$\overrightarrow{A}_{sy} = \left(\frac{1}{\rho_i h_i} \right) \left(\frac{\partial \sigma_{yy}}{\partial y} + \frac{\partial \sigma_{xy}}{\partial x} \right), \quad (59)$$

respectively, where σ is the internal ice stress tensor (kg s^{-2}). The components of the stress gradients $\frac{\partial \sigma_{xx}}{\partial x}$, $\frac{\partial \sigma_{yy}}{\partial y}$, $\frac{\partial \sigma_{xy}}{\partial x}$, and $\frac{\partial \sigma_{xy}}{\partial y}$ are computed by first calculating the components of the stress tensor at the ice particle positions and then linearly interpolating these values to four points surrounding each ice particle (Figure 6).

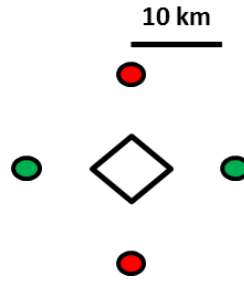


Figure 6. Schematic of the locations at which the ice stress tensor components are computed for calculation of the stress gradients. The white diamond represents an ice particle, the green circles represent the locations between which the zonal stress gradients are computed, and the red circles represent the locations between which the meridional stress gradients are computed. The stress gradient length scale is 10 km (image is slightly altered from original version in Lindsay and Stern, 2004).

In Figure 6, an ice particle is represented by the white diamond. The zonal components of the stress gradients, $\frac{\partial \sigma_{xx}}{\partial x}$ and $\frac{\partial \sigma_{xy}}{\partial x}$, are computed by finite differencing of the stress tensor values at the green circles, and the meridional components of the stress gradients, $\frac{\partial \sigma_{yy}}{\partial y}$ and $\frac{\partial \sigma_{xy}}{\partial y}$, are computed by finite differencing of the stress tensor values at the red circles.

The values of the stress tensor (kg m s^{-2}) are calculated as follows for each ice particle (*e.g.*, Gutfraind and Savage, 1997),

$$\begin{aligned} \sigma_{xx} &= P_i - 2\eta \left(\dot{\epsilon}_{xx} - 0.5(\dot{\epsilon}_{xx} + \dot{\epsilon}_{yy}) \right), \\ \sigma_{yy} &= \frac{\sigma_{xx}(1 - \sin(\phi_i))}{1 + \sin(\phi_i)}, \\ \sigma_{xy} &= -2\eta \dot{\epsilon}_{xy}, \end{aligned} \quad (60)$$

where P_i is the internal ice pressure (N m^{-2}), η is the ice viscosity ($\text{kg m}^{-1} \text{s}^{-1}$), $\dot{\epsilon}_{xx}$, $\dot{\epsilon}_{yy}$, and $\dot{\epsilon}_{xy}$ are the components of the strain rate tensor (s^{-1}), and ϕ_i is the internal ice friction angle (approximately 17.5°). The evaluation of σ_{yy} as a function of the other principal stress component, σ_{xx} , satisfies the Mohr-Coulomb yield criterion for a plastic regime as per Gutfraind and Savage, 1997. In Eq. (60), the pressure is taken as the ice compressive strength as per Hibler III, 1979 and Sayed et al., 2002 and is defined as,



$$P_i = P^* h_i e^{-20(1-A_{ice})}, \quad (61)$$

where P^* is a sea ice strength constant ($5.0 \times 10^3 \text{ N m}^{-2}$). The ice viscosity is defined as (e.g., Gutfraind and Savage, 1997),

$$\eta = \min\left(\frac{P_i \sin(\phi_i)}{\dot{\epsilon}_{xx} - \dot{\epsilon}_{yy}}, \eta_{max}\right), \quad (62)$$

where η_{max} is the maximum possible value of the ice viscosity ($1.0 \times 10^{11} \text{ kg m}^{-1} \text{ s}^{-1}$).

The components of the strain rate tensor are evaluated using the SPH formulation. While the strain rates for any given ice particle are theoretically influenced by all other ice particles in the model domain, it is most computationally practical to assume only a limited number of nearest-neighbor ice particles influence the strain rates of a given particle. In this paper, only the nearest three ice particles are considered when calculating strain rates for a given particle. Coastal boundary particles are considered when finding the nearest-neighbor particles, and their influence on the strain rates of nearby ice particles is treated the same as that from other ice particles. However, coastal cells have fixed zero-velocities and are assumed to be constantly circular with a radius of 5 km. They also exert an additional repulsive force on ice particles (see section 2.3.6).

The influence that a given ice particle exerts on another decreases exponentially with distance between particles, and is most commonly represented through the Gaussian kernel. The two-dimensional Gaussian kernel is defined as (e.g., Gutfraind and Savage, 1997),

$$W(\mathbf{r}, L) = \frac{1}{\pi L^2} e^{-\frac{r^2}{L^2}}, \quad (63)$$

where \mathbf{r} is the distance from the ice particle for which the strain rates are being calculated to a nearest-neighbor particle (m), and L is a smoothing length (150 km as per Lindsay and Stern, 2004). The components of the strain rate tensor are then given as (e.g., Gutfraind and Savage, 1997),

$$\begin{aligned} \dot{\epsilon}_{xx} &= \sum_k \left(-\frac{2I_{area_k}(u_k - u_i)W(r, L)_k r_{xk}}{L^2} \right), \\ \dot{\epsilon}_{yy} &= \sum_k \left(-\frac{2I_{area_k}(v_k - v_i)W(r, L)_k r_{yk}}{L^2} \right), \\ \dot{\epsilon}_{xy} &= \sum_k \left(\frac{-I_{area_k}(v_k - v_i)W(r, L)_k r_{yk} - I_{area_k}(u_k - u_i)W(r, L)_k r_{xk}}{L^2} \right), \end{aligned} \quad (64)$$

where I_{area_k} is the total surface area of the k^{th} nearest-neighbor ice particle (m^2), u_k and v_k are the zonal and meridional velocities of the k^{th} nearest-neighbor ice particles, respectively (m s^{-1}), u_i and v_i are the zonal and meridional velocities of the ice particle for which the strain rate tensor is being calculated, respectively (m s^{-1}), and r_{xk} and r_{yk} are the zonal and meridional distances from the ice particle for which the strain rates are being calculated to the k^{th} nearest-neighbor particle (m). The surface areas of the ice particles are calculated at each time-step using Voronoi tessellation over the whole model domain as per Lindsay and Stern, 2004. For each ice particle, the Voronoi polygon covers the area surrounding the particle which is closer to that particle than to any other.



526 2.3.6 Coastal boundary force

527 In order to prevent ice particles from drifting past the coastal boundary cells, a repulsive force from each coastal cell
 528 is exerted on every ice particle in the direction of the vector pointing from the coastal cell toward the ice particle. As
 529 per Lindsay and Stern, 2004, the force is given in the form $\frac{1}{R^2}$, where R is the distance from the coastal cell to the ice
 530 particle. The force is set to be 0.1 N m^{-2} at a distance of 25 km. An identical repulsion force is also exerted on ice
 531 particles from the boundaries of the model domain in the ocean in order to keep ice particles from drifting outside
 532 the model domain.

533 2.3.7 Dynamic evolution of ice thickness and concentration

534 Changes in the ice thickness and concentration of particles due to dynamics are determined by the principal
 535 components of the strain rate tensor as follows,

$$536 \quad \frac{\partial h_i}{\partial t} = -h_i(\dot{\epsilon}_{xx} + \dot{\epsilon}_{yy}),$$

$$537 \quad \frac{\partial A_{ice}}{\partial t} = -A_{ice}(\dot{\epsilon}_{xx} + \dot{\epsilon}_{yy}), \quad (65)$$

538 respectively. The dynamically induced changes in ice thickness and concentration are then added to any
 539 thermodynamically induced changes in these parameters at each time-step.

540 2.4 Time-stepping schemes

541 Several numerical integration schemes for time-stepping are used in the present model. The Euler-forward scheme
 542 (*e.g.*, Khandekar, 1980) is used to solve the thermodynamic equations for changes in snow and ice thickness (Eqs.
 543 50-52), changes in snow and ice temperature due to solar radiation penetration (Eqs. 18, 20-21), and snow
 544 accumulation. This scheme is used to calculate changes from the first to second time-step in melt-pond depth (Eq.
 545 22), water temperature beneath the base of the ice (Eq. 29), and lead area fraction (Eq. 27). The Euler-forward
 546 scheme is additionally used in the dynamic model to integrate the ice particle velocities to position displacements, to
 547 update the dynamically forced changes in ice thicknesses and concentrations (Eq. 65), and to integrate the initial ice
 548 accelerations to velocities from the first time-step to the second. The Euler-forward scheme is represented by,

$$549 \quad X_{i+1} = X_i + \Delta t \left(\frac{\partial F}{\partial t_i} \right); i = 1, \quad (66)$$

550 where X is the variable being solved, i is the time-step index, Δt is the time-step (seconds), and F is the function of
 551 X differentiated with respect to time, t .

552 The second-order Adams-Bashforth scheme (*e.g.*, Khandekar, 1980) is used to solve thermodynamic equations for
 553 changes in melt-pond depth (Eq. 22), water temperature beneath the base of the ice (Eq. 29), and lead area fraction
 554 (Eq. 27) from the second to the fourth time-steps. This scheme is also used to solve the changes in ice particle
 555 velocities from the second to the fourth time-steps in the dynamic model. The second-order Adams-Bashforth
 556 scheme is represented by,



$$X_{i+1} = X_i + \Delta t \left(1.5 \frac{\partial F}{\partial t_i} - 0.5 \frac{\partial F}{\partial t_{i-1}} \right); 1 < i \leq 3. \quad (67)$$

The fourth-order Adams-Bashforth scheme (*e.g.*, Matthews and Fink, 2004) is used to solve for changes in melt-pond depth (Eq. 22), water temperature beneath the base of the ice (Eq. 29), and lead area fraction (Eq. 27) from the fourth time-step onward in the thermodynamic model. In the dynamic model, the fourth-order Adams-Bashforth predictor-corrector scheme (*e.g.*, Matthews and Fink, 2004) is used to solve the ice velocity changes from the fourth time-step onward. The fourth-order Adams-Bashforth predictor-corrector scheme is represented by,

$$X_{i+1} = X_i + \frac{\Delta t}{24} \left(55 \frac{\partial F}{\partial t_i} - 59 \frac{\partial F}{\partial t_{i-1}} + 37 \frac{\partial F}{\partial t_{i-2}} - 9 \frac{\partial F}{\partial t_{i-3}} \right),$$

$$X_{i+1} = X_i + \frac{\Delta t}{24} \left(9 \frac{\partial F}{\partial t_{i+1}} + 19 \frac{\partial F}{\partial t_i} - 5 \frac{\partial F}{\partial t_{i-1}} + \frac{\partial F}{\partial t_{i-2}} \right); i > 3, \quad (68)$$

where the first line represents the fourth-order Adams-Bashforth scheme, and both lines represent the sequential steps of the combined predictor-corrector scheme.

The one-dimensional heat equations for the snow and ice temperatures (Eqs. 1 and 7) in the thermodynamic model are solved using the standard Euler-forward scheme and centred finite-differencing for second-order differential equations between the first and second time-steps, and the Dufort-Frankel algorithm (*e.g.*, EC93 and Mitchell and Griffiths, 1980) from the second time-step onward. The Euler-forward scheme with centred finite-differencing is represented by (*e.g.*, MacKinnon, 2015),

$$X_{i+1}^j = X_i^j + \frac{\kappa \Delta t}{\Delta z^2} (X_i^{j+1} - 2X_i^j + X_i^{j-1}); i = 1, \quad (69)$$

where j is the depth level index in the snow or ice layer, κ is the quotient of the thermal conductivity and the volumetric heat capacity for snow or ice, and Δz is the spacing between depth levels (m). The Dufort-Frankel algorithm is represented by (*e.g.*, MacKinnon, 2015),

$$X_{i+1}^j = \left(\frac{1-\beta}{1+\beta} \right) X_{i-1}^j + \left(\frac{\beta}{1+\beta} \right) (X_i^{j+1} + X_i^{j-1}), \quad (70)$$

where β represents the quantity $2 \frac{\kappa \Delta t}{\Delta z^2}$.

Acceptable numerical stability of the integration schemes is achieved when a time-step Δt of one hour (3600 seconds) is used for the thermodynamic model-only runs, and a time-step of one minute (60 seconds) is used for the thermodynamic-dynamic coupled model runs.

2.5 Model input

The atmospheric inputs to the model include the 2 m air and dew-point temperatures, relative humidity, 10 m wind speed and direction, surface pressure, total cloud cover area fraction, snowfall, and total precipitation. All atmospheric parameters except for precipitation are taken from the North American Regional Reanalysis (NARR), which has an approximately 0.3° spatial resolution (about 33.3 km) and a three-hourly temporal resolution. In order



to make the wind speed more realistic for near surface winds, a logarithmic wind profile law is used to scale the 10 m height wind speeds to 2 m (*e.g.*, ISO 19901-1),

$$U_a = U_{a_{10m}} \left(1 + 0.0573 \sqrt{1 + 0.15 U_{a_{10m}}} \right) \ln \left(\frac{2}{10} \right), \quad (71)$$

where $U_{a_{10m}}$ is the NARR wind speed at 10 m (m s^{-1}).

The snowfall and total precipitation data are given in meters of water equivalent over the dataset time-step and are taken from the European Centre for Medium-Range Weather Forecasting (ECMWF) ERA-Interim Reanalysis, which has a 0.5° - 0.75° spatial resolution (about 55.5-83 km) and a six-hourly temporal resolution. Rainfall is assumed to be the difference of the total precipitation and the snowfall. In order to convert the ECMWF snowfall data from meters of water equivalent to actual snow accumulation, SF , the following relationship to 2 m air temperature is used (*e.g.*, NWS, 1996),

$$\begin{aligned} SF &= 5SF_w, T_a \geq 0, \\ SF &= 10SF_w, 0 > T_a \geq -1.1, \\ SF &= 15SF_w, -1.1 > T_a \geq -3.9, \\ SF &= 20SF_w, -3.9 > T_a \geq -7.8, \\ SF &= 30SF_w, -7.8 > T_a \geq -11.1, \\ SF &= 40SF_w, -11.1 > T_a \geq -15, \\ SF &= 50SF_w, T_a < -15, \end{aligned} \quad (72)$$

where SF_w is the snowfall rate in meters of water equivalent (m s^{-1}), and T_a is in $^\circ\text{C}$.

The ice and oceanographic inputs to the model include the sea surface temperature, sea surface salinity, surface current speed and direction, sea surface height above the geoid, and sea ice thickness, concentration, and drift speed and direction. The ice and oceanographic parameters are taken from the Operational Mercator global Ocean analysis and forecast system. This dataset has a 0.08° spatial resolution (approximately 8.9 km), a two-hourly temporal resolution for sea surface temperature, sea surface salinity, and surface current speed and direction, and a daily-mean temporal resolution for sea surface height above the geoid, and sea ice thickness, concentration, and drift speed and direction. In this dataset, the sea surface temperature, salinity, currents, and height are initially derived from the Nucleus for European Models of the Ocean (NEMO 3.1), while the sea ice thickness, concentration, and velocity are derived from the LIM2 sea ice model. Sea surface height anomaly data derived from the Jason2, Cryosat, and Saral-Altika satellites are assimilated into the dataset, as well as sea surface temperature data from the Reynolds AVHRR-AMSR $\frac{1}{4}^\circ$ satellite, and in-situ profiles of ocean temperature and salinity. The sea ice thickness, concentration, and velocity are used to initialize the model, while the remaining metocean parameters described above are used to force the model for the duration of a run.



Finally, the Labrador coastal boundaries are included, and well as the ocean bathymetry (*e.g.*, GEBCO, 2008, 30-second data). All dynamic input data are spatially and temporally linearly interpolated as needed.

2.6 Comparison of LIM2 sea ice data with CIS ice charts

Given the fact that the LIM2 sea ice dataset used here to initialize the model and compare model results to the “best estimate” of sea ice conditions is itself derived from a model, it is worth comparing the LIM2 ice data from the current model run period of April-May 2015 for the Labrador coast with observations from the CIS ice charts. The LIM2 dataset was used in this study due to its relatively high temporal (daily) resolution compared to the weekly-mean resolution of the CIS digitized ice charts. Figure 7-Figure 15 show the normalized errors between the weekly average CIS chart and the LIM2 ice concentration and thickness for April-May 2015 for central coastal Labrador from Makkovik north to Nain. Here, the normalized (dimensionless) error is defined as,

$$E_{C,T} = \frac{CIS_{C,T} - LIM2_{C,T}}{CIS_{C,T}}, \quad (73)$$

where $CIS_{C,T}$ is the ice concentration (0-1) or thickness (m) of a given domain grid point from the CIS chart, and $LIM2_{C,T}$ is the ice concentration (0-1) or thickness (m) of the same grid point from the LIM2 dataset.

Figure 7-Figure 15 show that the LIM2 dataset is fairly close to the CIS charts in terms of ice concentration and thickness for this period in the areas of the model domain closer to shore. The LIM2 dataset simulates greater ice concentrations and thicknesses further offshore than the CIS charts show. However, the present paper focuses on simulating ice conditions close to the Labrador coast from near Makkovik up to Nain; hence the LIM2 dataset can be considered reliable for the purposes of this study. Note that the LIM2 model does not simulate the land-fast ice cover directly along the shoreline, whereas the CIS charts show the land-fast ice. However, in this paper, the break-up of the land-fast ice is assumed to occur when the deployed buoys began to drift.

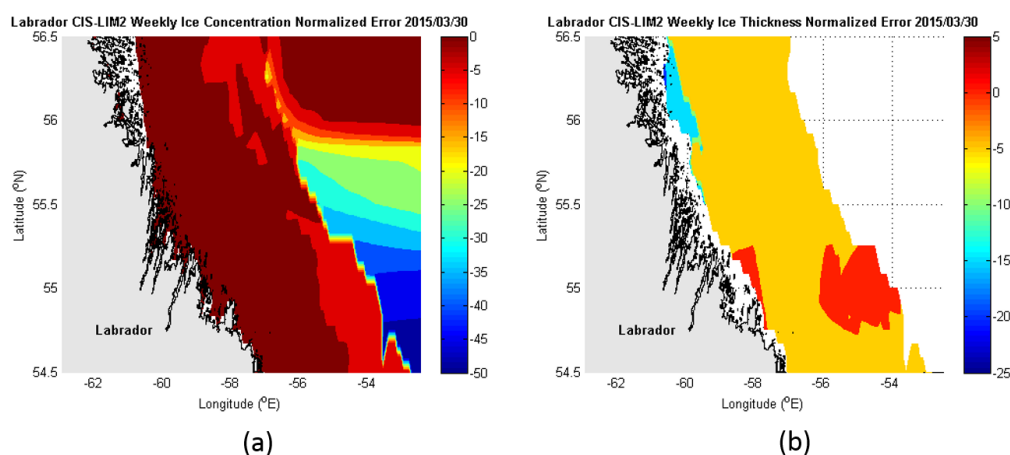
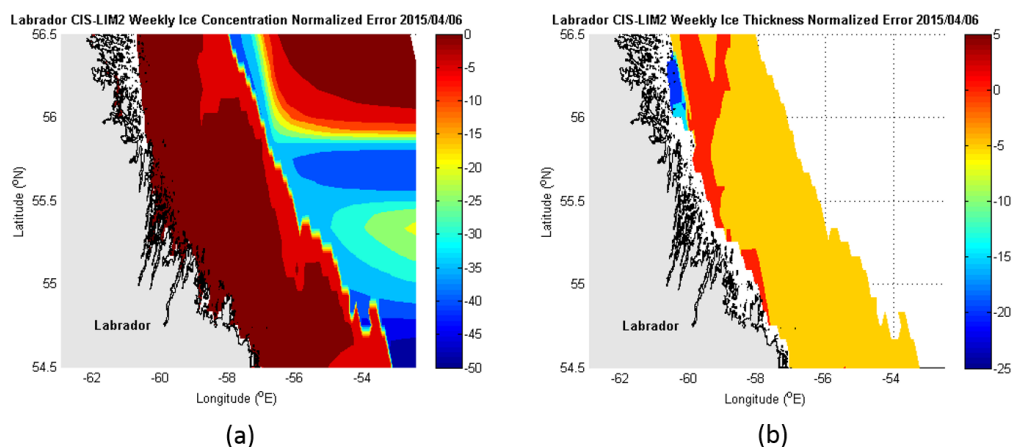
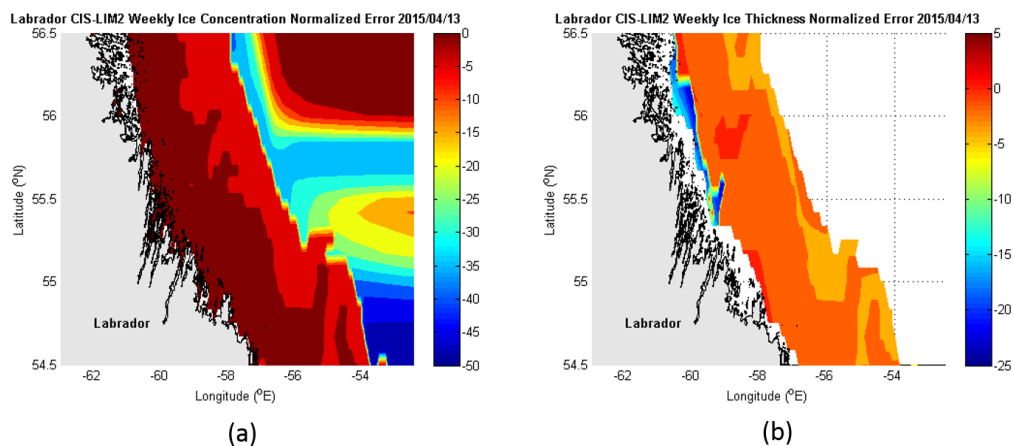


Figure 7. Central coastal Labrador weekly average CIS-LIM2 ice concentration (a) and thickness (b) normalized error for the week of March 30 – April 5, 2015.



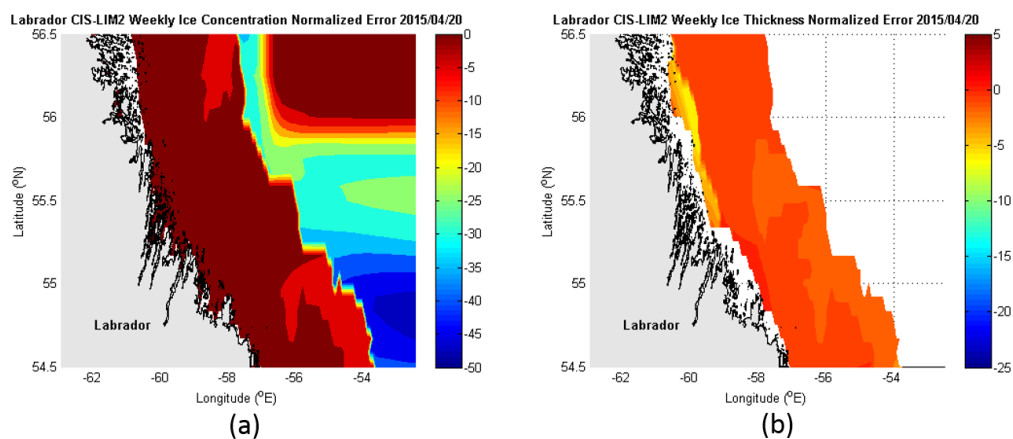
640

641 **Figure 8.** Central coastal Labrador weekly average CIS-LIM2 ice concentration (a) and thickness (b) normalized
 642 error for the week of April 6-12, 2015.

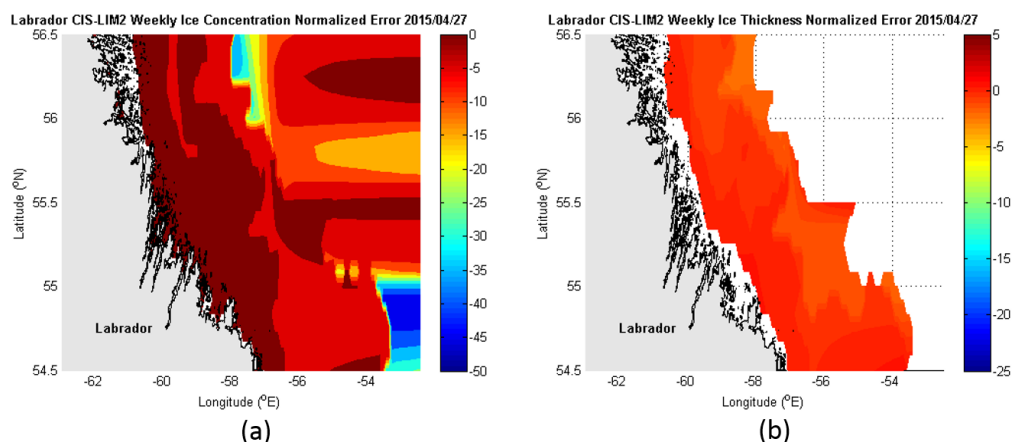


643

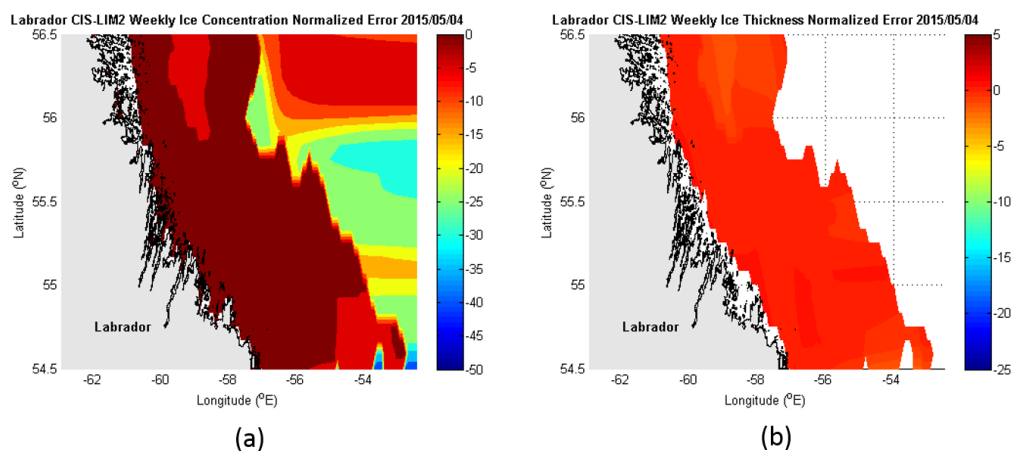
644 **Figure 9.** Central coastal Labrador weekly average CIS-LIM2 ice concentration (a) and thickness (b) normalized
 645 error for the week of April 13-19, 2015.



646
 647 **Figure 10.** Central coastal Labrador weekly average CIS-LIM2 ice concentration (a) and thickness (b) normalized
 648 error for the week of April 20-26, 2015.

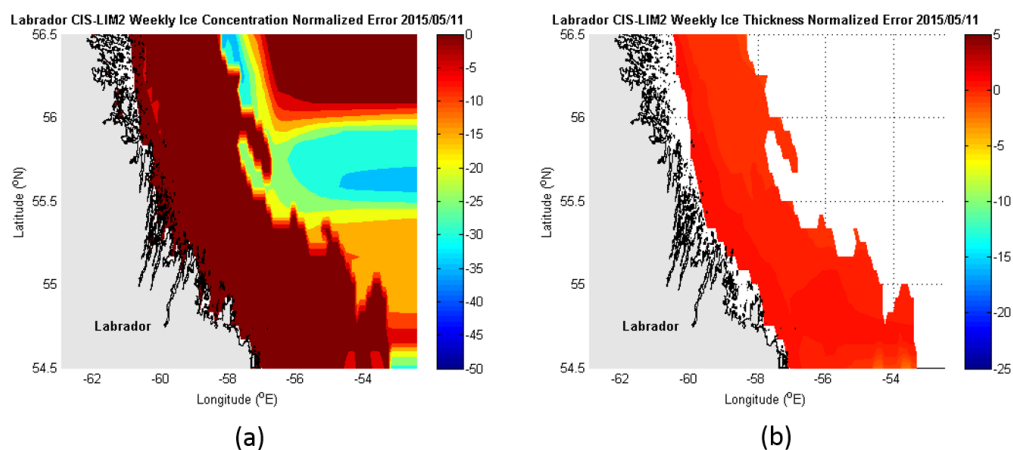


649
 650 **Figure 11.** Central coastal Labrador weekly average CIS-LIM2 ice concentration (a) and thickness (b) normalized
 651 error for the week of April 27 – May 3, 2015.



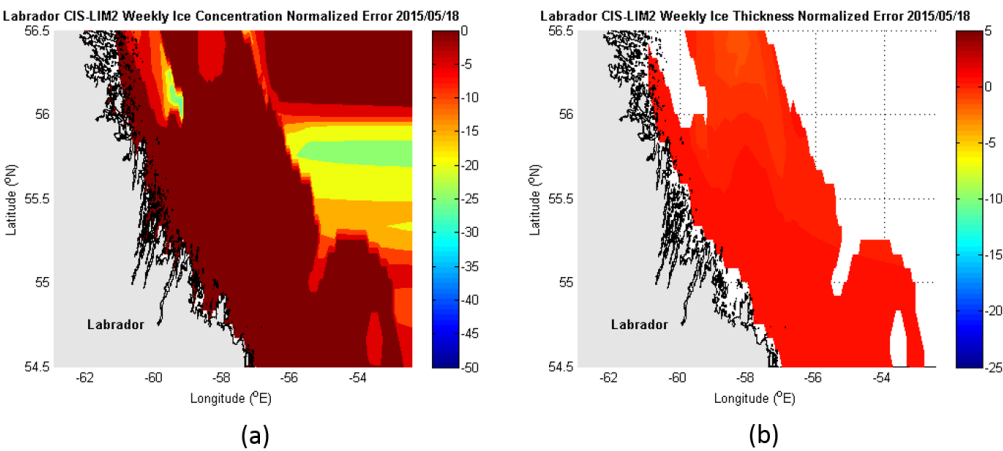
652

653 **Figure 12.** Central coastal Labrador weekly average CIS-LIM2 ice concentration (a) and thickness (b) normalized
 654 error for the week of May 4-10, 2015.

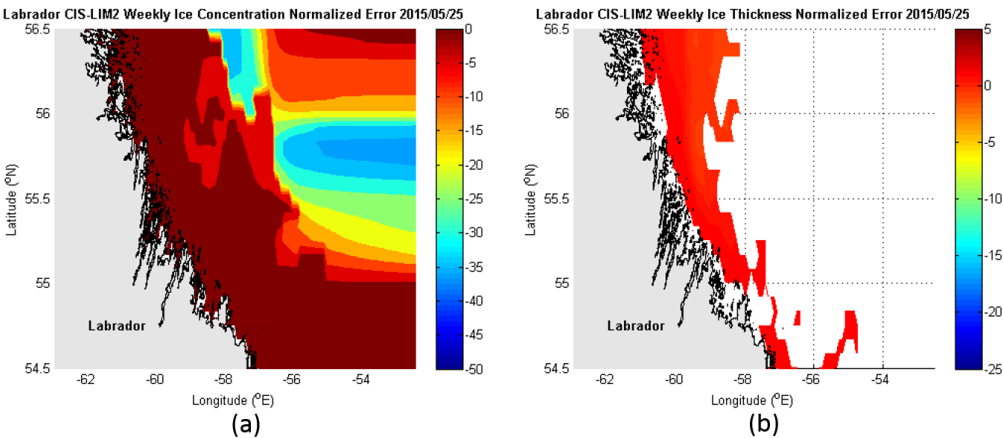


655

656 **Figure 13.** Central coastal Labrador weekly average CIS-LIM2 ice concentration (a) and thickness (b) normalized
 657 error for the week of May 11-17, 2015.



658
659 **Figure 14.** Central coastal Labrador weekly average CIS-LIM2 ice concentration (a) and thickness (b) normalized
660 error for the week of May 18-24, 2015.



661
662 **Figure 15.** Central coastal Labrador weekly average CIS-LIM2 ice concentration (a) and thickness (b) normalized
663 error for the week of May 25-31, 2015.

664 **3 Model Validation**

665 In this section, results of model runs are presented for the thermodynamic model for April 1 – May 31, 2015, as well
666 as runs of the coupled thermodynamic-dynamic model for May 1-7, 2015. The thermodynamic model run period
667 was selected to cover the observed break-up periods for the land-fast ice offshore Makkovik and Nain. Two of the
668 three ice drift tracking buoys deployed offshore Makkovik began to drift on April 23 (Figure 1), and each of the
669 three buoys deployed offshore Nain began to drift on May 1, 2, and 6, respectively. The shorter thermodynamic-



dynamic model run period was selected to cover most of the observed break-up period for the land-fast ice offshore Nain.

The model runs are initialized with the best estimate of sea ice conditions over the model domain as obtained from the LIM2 sea ice model dataset, and model results here are compared with the LIM2 data. Hereafter, all results from the model presented in this paper are referred to as “model” results, and data from the LIM2 dataset are referred to explicitly. The model domain extends between 62°W and 57.5°W longitude and 55°N and 57°N latitude. For the thermodynamic model-only runs, the parameters of interest which are presented here are the sea ice thickness and concentration. For the thermodynamic-dynamic model, the sea ice thickness, concentration, and velocity are presented. Of particular interest in the present work is the model performance in the regions offshore Makkovik and Nain; hence, additional analyses are given for the temporal evolution of sea ice thickness and concentration in these areas.

The thermodynamic model runs use a 0.45° spatial resolution (approximately 50 km) for initial ice particle spacing and a one-hourly temporal resolution, while the thermodynamic-dynamic model run uses a 0.5° spatial resolution (approximately 55.5 km) for initial ice particle spacing and a one-minute temporal resolution. The higher temporal resolution is needed for the stability of the numerical integration scheme in the dynamic model. Hence, a lower spatial resolution and shorter model run period are used for the dynamic model to lessen the required computation time.

3.1 Thermodynamic model results

The largest uncertainty in the thermodynamic model is the initialization of snow cover on the sea ice. While available reanalysis datasets provide snow depth, they only provide it in meters of water equivalent; however, actual snow depth on the sea ice plays a critical role in the evolution of the ice cover due to the strong insulating effect of snow. Since there do not exist any widespread and frequent snow depth measurements along the Labrador coast, an approximate early spring mean snow depth value of 40 cm is used here to initialize the model on April 1. This depth was taken from measurements of snow depth performed on Lake Melville in March 2009 (*e.g.*, Prinsenberg et al., 2011). It cannot be overstated how uncertain this initial snow depth value is, as it is applied to the entire model domain, and snow depths may be significantly greater further north around Nain. Future use of this model for operational ice forecasting purposes must involve adequate snow depth data acquisition.

In the model results presented here, one model run assumes 40 cm of snow depth over the entire model domain at the start of April 1, 2015, while another model run assumes no snow on the sea ice at the start of the model run on April 1. Both model runs are subject to the same snow accumulation on the ice over the two-month period as forced by the ECMWF snowfall data. Hence, the effect of a significant snow cover on the ice at the start of the melt season can be examined.

Figure 16 shows the initial ice conditions on April 1, 2015 00:00 UTC as given by the LIM2 dataset. The green circle represents the region offshore Makkovik analyzed here, and the purple circle represents the region offshore Nain. There are four model grid points within each of these circled regions over which ice thickness and



concentrations are averaged for the offshore Makkovik and Nain analyses. These two regions were selected to encompass the land-fast ice in the vicinities of Makkovik and Nain so that the timing of the land-fast ice break-up could be modeled and compared with the actual timing of the break-up as recorded by the ice tracking buoys.

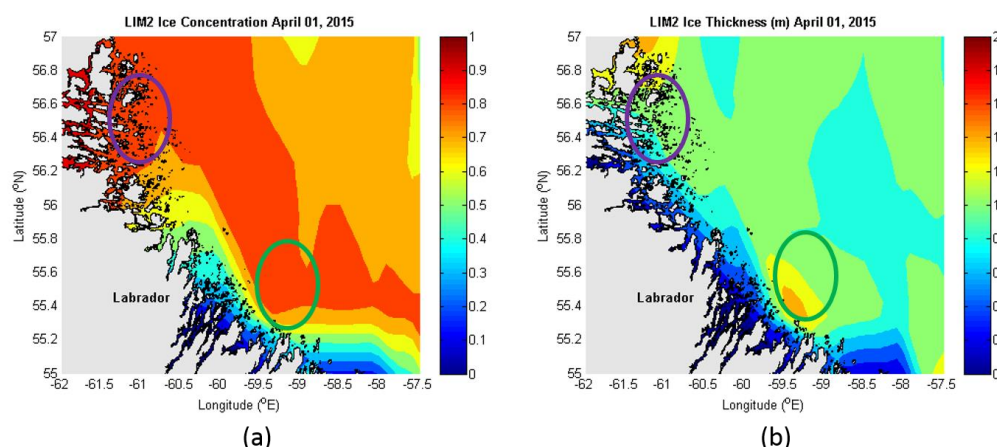


Figure 16. Sea ice concentration (a) and thickness (b) over the model domain at the start of the thermodynamic model runs on April 1, 2015 00:00 UTC, as obtained from the LIM2 dataset. The region circled in green represents the area over which ice conditions offshore Makkovik are analyzed in this section, and the purple circled region represents the area over which ice conditions offshore Nain are analyzed.

Figure 17 shows the evolution of average ice conditions during April 1 – May 31, 2015 in the regions offshore Makkovik (green circles in Figure 16) and Nain (purple circles in Figure 16) according to the LIM2 data, the thermodynamic model with 40 cm of initial snow cover, and the thermodynamic model with no initial snow cover. According to the model run with initial snow cover, the average ice thickness and concentration offshore Makkovik decrease to zero on May 14, while for the run with no initial snow cover, the ice disappears completely around Makkovik on May 1. The progression of the LIM2 ice thickness and concentration near Makkovik shows a somewhat less precipitous decline in ice conditions compared to the model results shown here. While the LIM2 ice thickness and concentration do not reach zero during the model time period, they decline to less than 0.2 m and 0.1, respectively, by May 18 before rebounding slightly as more ice drifts into the region from the north. This minimum in overall average ice conditions offshore Makkovik occurs four days after the model minimum with 0.4 m initial snow cover, and 18 days after the disappearance of ice in the model run with no initial snow cover. In the region offshore Nain, the ice also disappears on May 14 in the model with initial snow cover, and on April 25 in the model without initial snow cover (Figure 17). The LIM2 ice thickness and concentration decrease to zero by May 15.

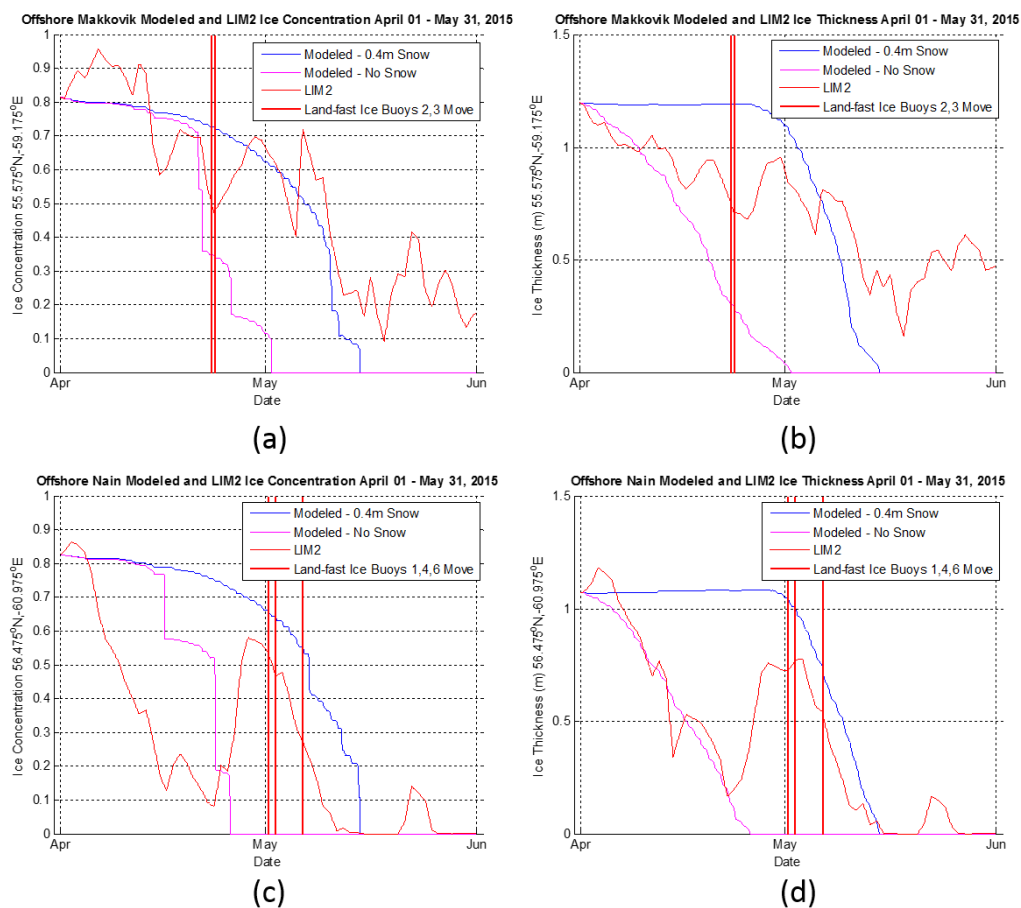


Figure 17. Evolution of average ice concentration (a,c) and thickness (b,d) in the focus regions offshore Makkovik (a,b) and Nain (c,d) during April 1 – May 31, 2015. The thin red lines represent LIM2 ice conditions, the blue lines represent ice conditions for the thermodynamic model presented here initialized with 40 cm of snow, and the magenta lines represent ice conditions for the thermodynamic model initialized with no snow. The thick red lines mark the timing of first recorded movement by the land-fast ice buoys. The latitude-longitude coordinates shown on the y-axes represent the central locations for the regions over which average ice conditions are shown.

The thick red lines in Figure 17 mark the times that the land-fast ice buoys first recorded movement, indicating that the break-up of the land-fast ice in those regions had begun. Buoys 2 and 3 began to drift on April 23 around 05:00 and 15:00 UTC, respectively, offshore Makkovik, and buoys 1, 4, and 6 began to drift around May 1 10:00, May 2 12:00, and May 6 12:00 UTC, respectively, offshore Nain. The model run with 40 cm initial snow cover most accurately predicts the timing of the onset of the land-fast ice break-up with precipitous declines in regional mean ice thickness and concentration commencing immediately after these times. The averaged results for both the Makkovik and Nain regions suggest that there was most likely significant snow cover on the ice on April 1, and that



740 if the model is properly initialized with snow cover conditions, it can reasonably predict the progression and timing
741 of the decline in regional ice concentration and thickness more than a month in advance.

742 At the specific locations at which the ice drift buoys were deployed, Figure 18 shows the modeled ice concentrations
743 and thicknesses near Makkovik and Nain for April 1 – May 31 from the thermodynamic model with 0.4 m of initial
744 snow cover. This model run is not initialized with the LIM2 ice concentration and thickness data, but rather assumes
745 the land-fast ice at these five locations had a concentration and thickness of 0.995 and 0.95 m on April 1,
746 respectively. The assumed ice thickness represents the mean of the normal thickness range for medium first-year ice
747 (0.7-1.2 m), which was the ice type shown for these locations on April 1 on the CIS daily ice charts. In Figure 18,
748 the times at which the modeled ice concentrations first drop below 0.99 and the modeled thicknesses first began to
749 display steep decreases below their original thickness of 0.95 m are used as proxies for the beginning of the local of
750 land-fast ice break-up. These times fall within 4.7 hours to 5.9 days from the times at which the drift buoys began to
751 move at these locations (Table 4).

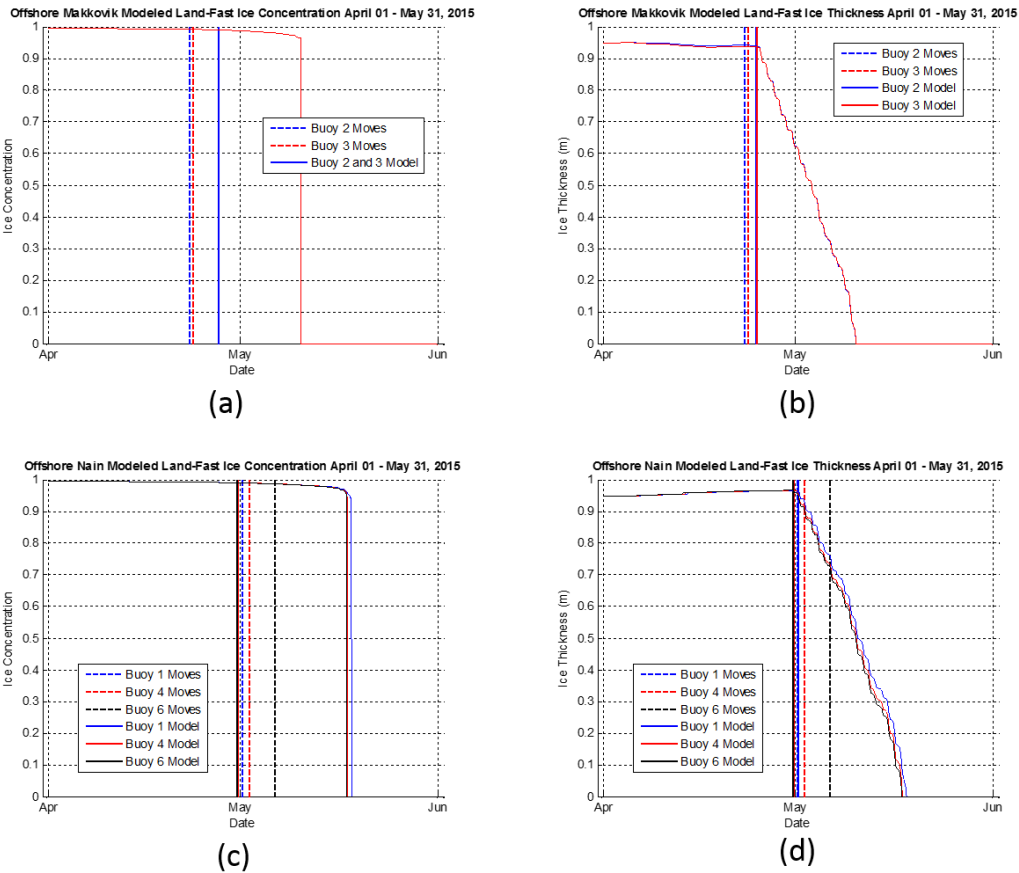


Figure 18. Modeled ice concentration and thickness (thin solid lines) vs. time at the buoy deployment locations near Makkovik (a,b) and Nain (c,d). The vertical dashed lines represent the times at which the buoys first recorded motion, the vertical solid lines represent the times at which the modeled ice concentrations begin to fall below 0.99 (a,c), and the times at which the modeled ice thicknesses first fall below 0.95 m (all times in UTC).

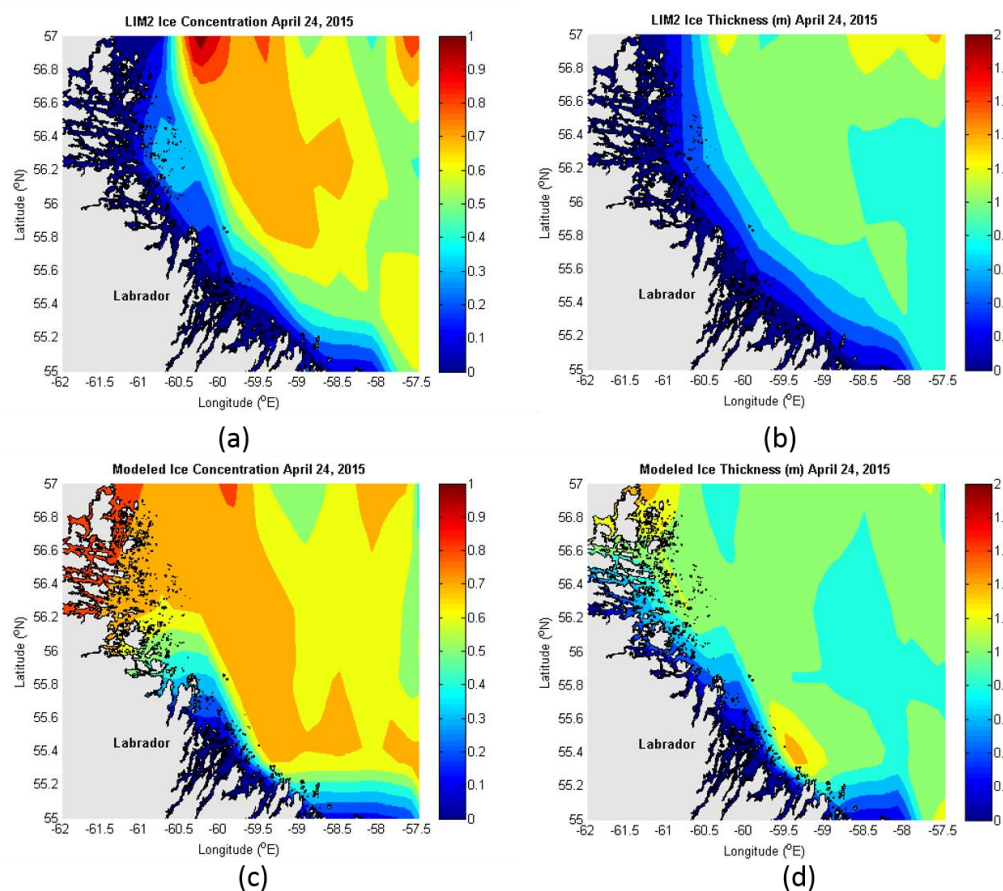
Table 4. Summary of buoy deployment locations, modeled and observed land-fast ice break-up times according to concentration and thickness criteria described above, and observed minus modeled break-up time error ranges.

Buoy	Deployment Coordinates	Modeled Break-Up Time (Thickness)	Modeled Break-Up Time (Concentration)	Observed Break-Up Time	Observed - Modeled Error Range (hours)
1	56.45°N, 60.78°W	May 01 14:00	April 30 17:00	May 01 09:18	-4.7 to 16.3



2	55.29°N, 59.24°W	April 24 21:00	April 27 14:00	April 23 04:32	-105.5 to -40.5
3	55.28°N, 59.19°W	April 25 02:00	April 27 14:00	April 23 14:14	-95.8 to -35.8
4	56.40°N, 60.80°W	April 30 20:00	April 30 16:00	May 02 11:26	39.4 to 43.4
6	56.39°N, 60.84°W	April 30 18:00	April 30 15:00	May 06 11:38	137.6 to 140.6

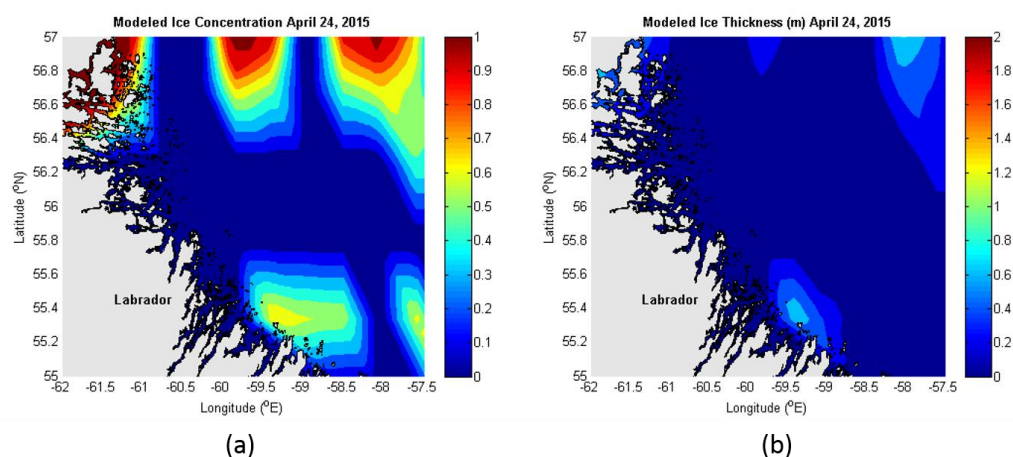
Figure 19 shows contour plots of the modeled and LIM2 ice thickness and concentration across the model domain 24 days into the model run, and one day after the first land-fast ice buoys offshore Makkovik began to drift. The model results shown in Figure 19 are from the run initialized with 0.4 m of snow cover. The model shows little change in ice thicknesses by April 24 compared to April 1, with some decrease in ice concentrations. The LIM2 data show a comparatively more extensive retreat in ice thicknesses and concentrations by April 24; however, both the LIM2 data and the model results show a large region of ice concentrations around 0.7 toward the coast, with concentrations around 0.6 immediately to the east.



766

767 **Figure 19.** Sea ice concentration (a,c) and thickness (b,d) on April 24, 2015 03:00 UTC (00:00 AST) from LIM2
 768 data (a,b) and the thermodynamic model presented here (c,d). The results of the thermodynamic model run shown
 769 here are initialized with 40 cm of snow.

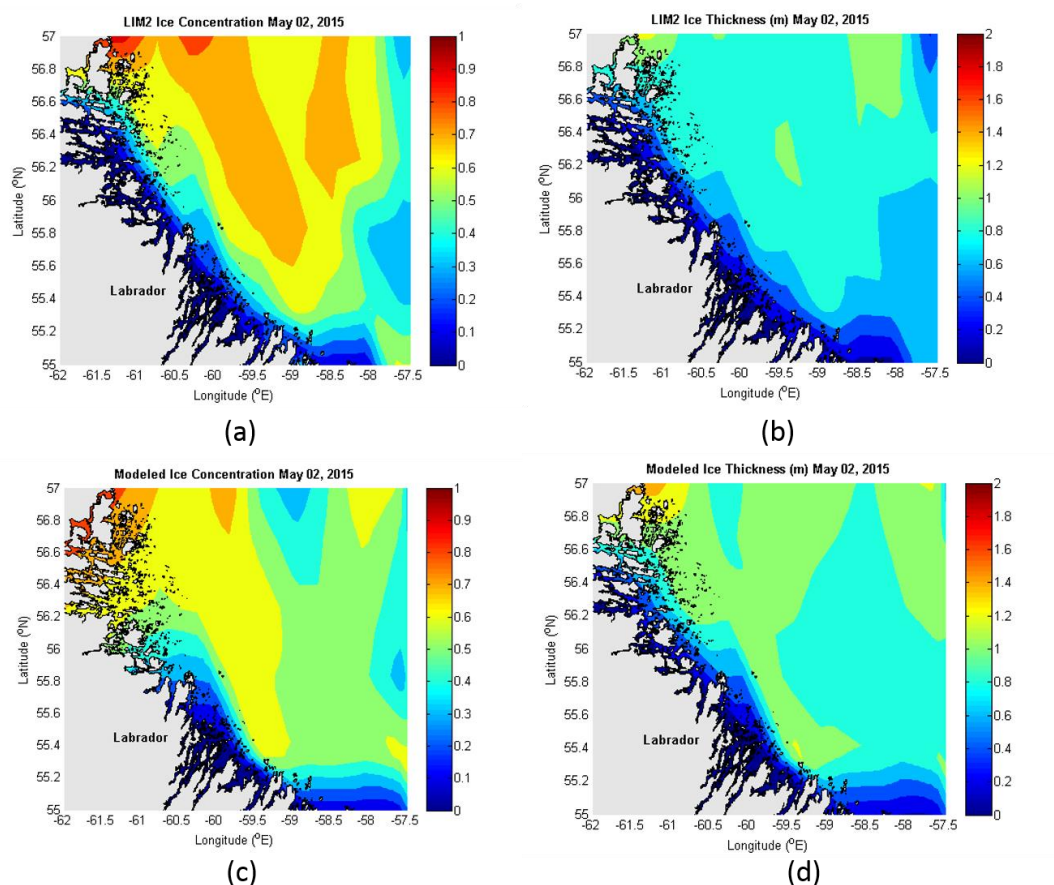
770 The results in Figure 20 show that when the thermodynamic model is initialized with no snow cover on April 1,
 771 nearly all the ice disappears by April 24. In this model run, the ice disappears completely from the model domain by
 772 May 2, which indicates that it is not a realistic scenario to initialize the model without a snow cover.



773

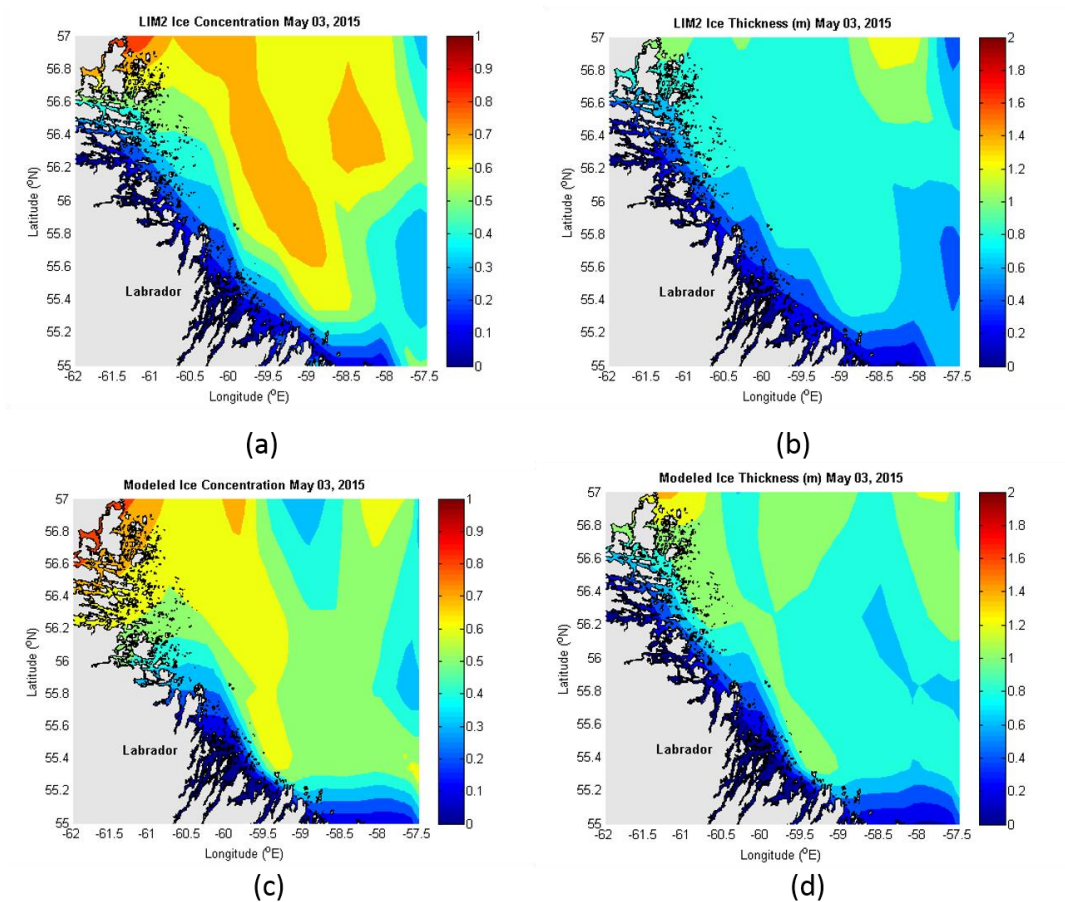
774 **Figure 20.** Sea ice concentration (a) and thickness (b) on April 24, 2015 03:00 UTC (00:00 AST) from the
 775 thermodynamic model with no initial snow cover.

776 Figure 21-Figure 23 show contour plots of the modeled and LIM2 ice thickness and concentration across the model
 777 domain for May 2, 3, and 7, respectively. These dates were selected to coincide with the timing of the first detected
 778 motion of the land-fast ice buoys deployed offshore Nain. These buoys began to drift on May 1, 2, and 6. The model
 779 results shown here are all from the run initialized with 0.4 m of snow cover. While the modeled results and LIM2
 780 data show somewhat different patterns of ice retreat during the May 2-7 period, both show a general pattern of the
 781 retreat of thicker, more concentrated ice toward the northern end of the model domain.



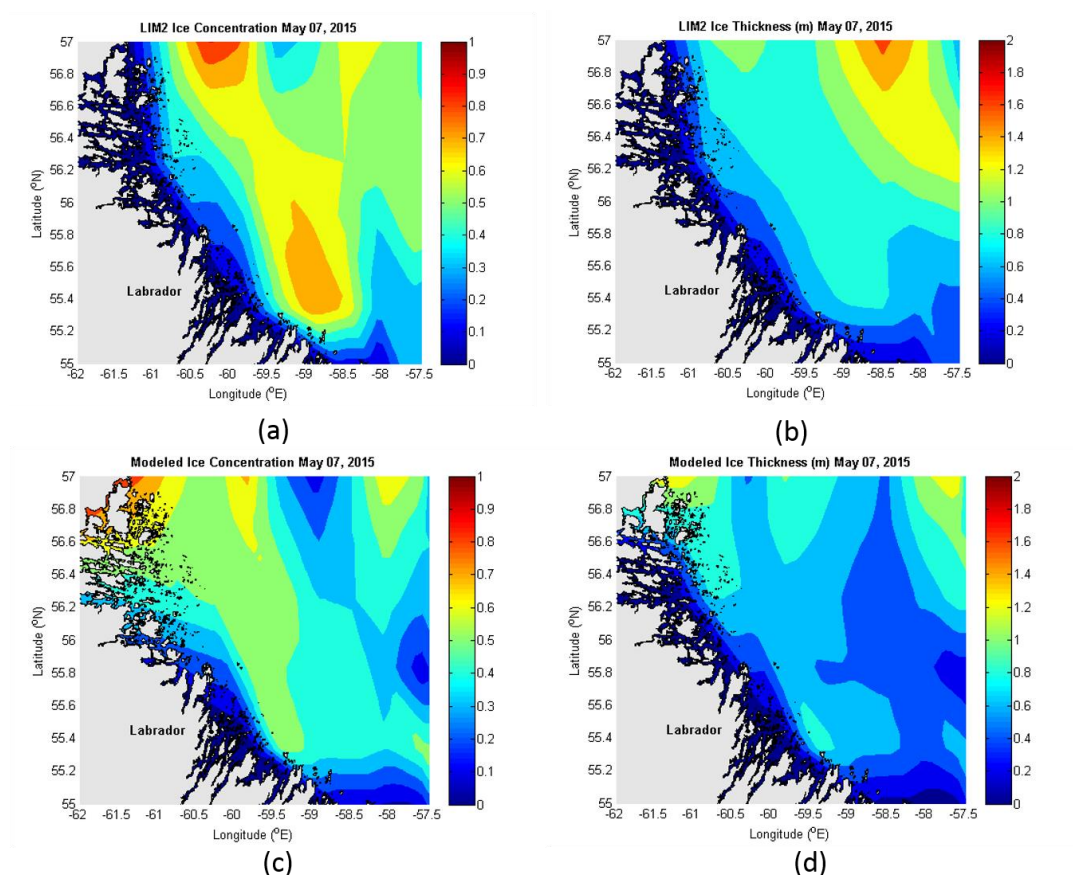
782

783 **Figure 21.** Sea ice concentration (a,c) and thickness (b,d) on May 02, 2015 03:00 UTC (00:00 AST) from LIM2
 784 data (a,b) and the thermodynamic model presented here (c,d). The results of the thermodynamic model run shown
 785 here are initialized with 40 cm of snow.



786

787 **Figure 22.** Sea ice concentration (a,c) and thickness (b,d) on May 03, 2015 03:00 UTC (00:00 AST) from LIM2
 788 data (a,b) and the thermodynamic model presented here (c,d). The results of the thermodynamic model run shown
 789 here are initialized with 40 cm of snow.



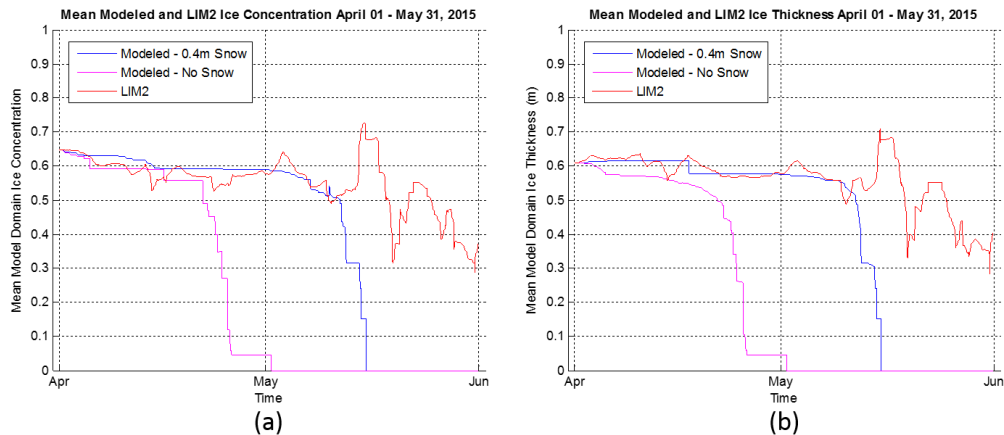
790

791 **Figure 23.** Sea ice concentration (a,c) and thickness (b,d) on May 07, 2015 03:00 UTC (00:00 AST) from LIM2
 792 data (a,b) and the thermodynamic model presented here (c,d). The results of the thermodynamic model run shown
 793 here are initialized with 40 cm of snow.

794 Figure 24 shows the evolution of average ice conditions during April 1 – May 31, 2015 over the model domain
 795 according to the LIM2 data, the thermodynamic model with 40 cm of initial snow cover, and the thermodynamic
 796 model with no initial snow cover. The spatially averaged ice thickness and concentration for the model run with 0.4
 797 m of initial snow cover tracks closely to the LIM2 mean thickness and concentration, and begins to decrease
 798 significantly on May 11 when both the mean thickness and concentration decrease to less than 0.5 (m or
 799 concentration). The ice disappears completely from the model domain on May 15. The spatially averaged ice
 800 thickness and concentration for the model run with no initial snow cover tracks closely to the LIM2 mean thickness
 801 and concentration, and begins to decrease significantly on April 21 when both the mean thickness and concentration
 802 decrease to less than 0.5 (m or concentration). In the model run with no initial snow cover, the ice disappears
 803 completely on May 1. The LIM2 mean domain ice thickness and concentration both remain fairly constant around



804 0.6 (m or concentration) during April 1 – May 11, and subsequently begin to display greater variability between 0.3-
805 0.7 (m or concentration) while showing an overall decrease, until May 31.



806
807 **Figure 24.** Evolution of average ice concentration (a) and thickness (b) over the entire model domain during April 1
808 – May 31, 2015. The red lines represent LIM2 ice conditions, the blue lines represent ice conditions for the
809 thermodynamic model presented here initialized with 40 cm of snow, and the magenta lines represent ice conditions
810 for the thermodynamic model initialized with no snow.

811 Table 5 summarizes the model domain mean ice thicknesses and concentrations for the selected dates shown in
812 Figure 19-Figure 23 for the LIM2 dataset, the model run with 0.4 m of initial snow cover, and the model run with no
813 initial snow cover.

814 **Table 5.** Summary of modeled vs. LIM2 model domain mean ice concentration and thickness for selected dates for
815 April 1 – May 31, 2015 model run.

Modeled vs. LIM2 Mean Domain Ice Concentration and Thickness (Thermodynamic Model)					
Date	April 01 Snow Cover (m)	LIM2 Concentration	Modeled Concentration	LIM2 Thickness (m)	Modeled Thickness (m)
April 24	0.40	0.42	0.57	0.43	0.48
	0.00		0.44		0.43
May 02	0.40	0.77	0.54	0.65	0.47
	0.00		0.00		0.00
May 03	0.40	0.78	0.53	0.69	0.47
	0.00		0.00		0.00

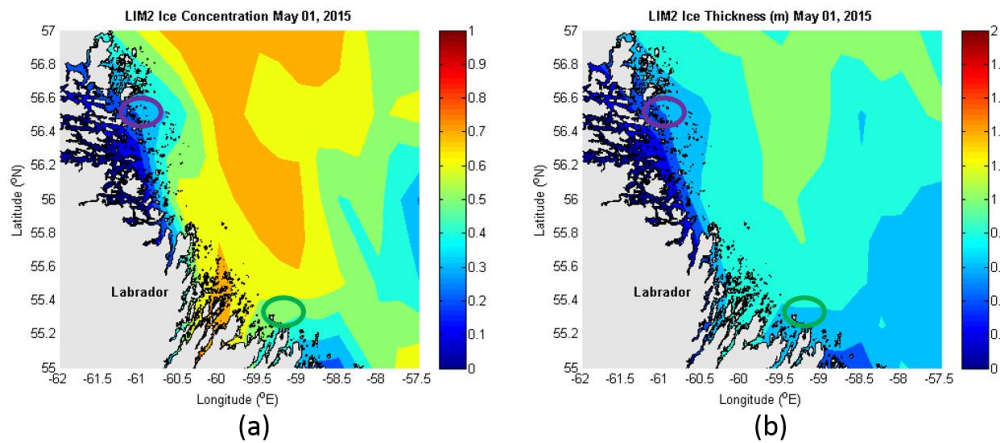


May 07	0.40	0.36	0.46	0.39	0.45
	0.00		0.00		0.00

816

817 **3.2 Thermodynamic-dynamic model results**

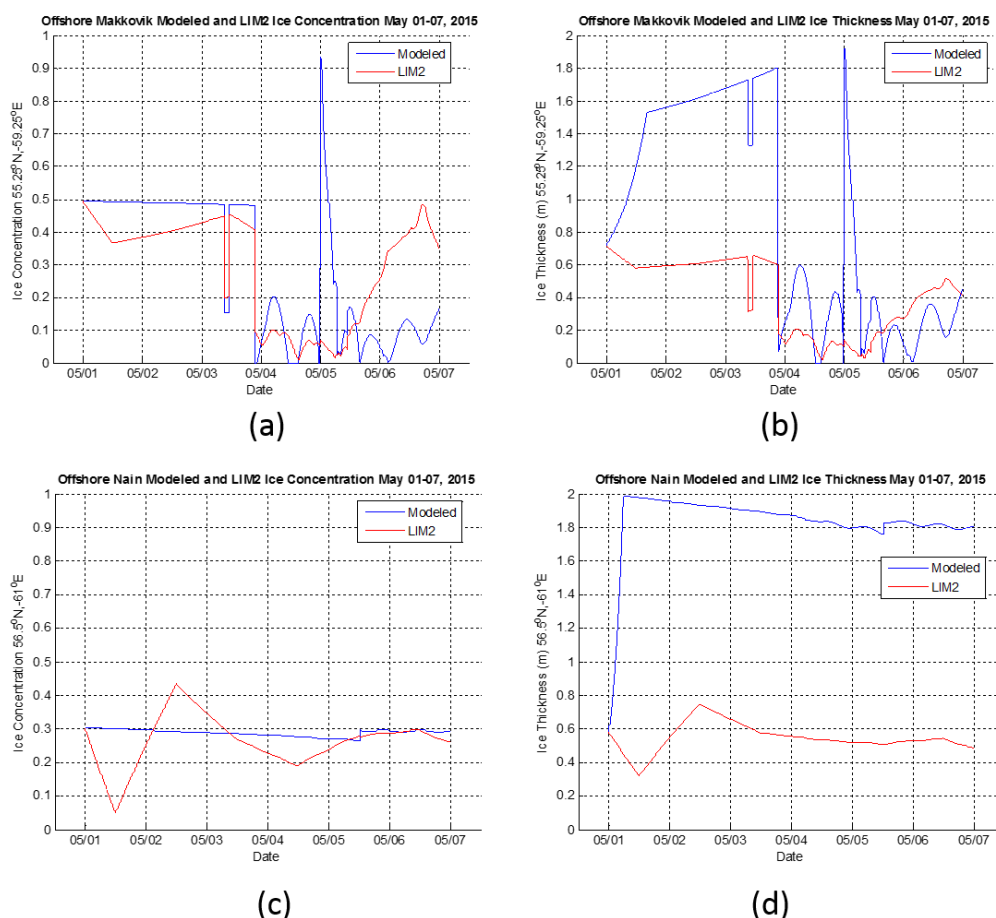
818 The coupled thermodynamic-dynamic model run for May 1-7, 2015 is initialized with the LIM2 ice thickness,
819 concentration, and velocity grid for May 1 00:00 UTC (Figure 25). The green circle represents the single coordinate
820 offshore Makkovik analyzed here (55.25°N, 59.25°W), and the purple circle represents the coordinate offshore Nain
821 (56.5°N, 61°W). Given that the ice particles are free to drift from their initial positions in the dynamic model, the
822 modeled ice conditions at these coordinates are linearly interpolated.



823

824 **Figure 25.** Sea ice concentration (a) and thickness (b) over the model domain at the start of the thermodynamic-
825 dynamic model run on May 1, 2015 00:00 UTC, as obtained from the LIM2 dataset. The region circled in green
826 represents the area over which ice conditions offshore Makkovik are analyzed in this section, and the purple circled
827 region represents the area over which ice conditions offshore Nain are analyzed.

828 Figure 26 shows the evolution of modeled and the LIM2 ice thickness (a,c) and concentration (b,d) during May 1-7
829 offshore Makkovik (a,b) and Nain (c,d).



830

831 **Figure 26.** Evolution of average ice concentration (a,c) and thickness (b,d) in the focus regions offshore Makkovik
 832 (a,b) and Nain (c,d) during May 1-7, 2015. The red lines represent LIM2 ice conditions, and the blue lines represent
 833 ice conditions for the thermodynamic-dynamic model. The latitude-longitude coordinates shown on the y-axes
 834 represent the central locations for the regions over which average ice conditions are shown.

835 Figure 27-Figure 30 show the modeled ice drift velocities and total speeds along the trajectories of buoys 1-4 during
 836 May 1-7. The plots for buoy 4 begin on May 2 when the buoy began to record drift (Figure 30). Results for buoys 5-
 837 6 are not shown because buoy 5 remained stationary on the land-fast ice offshore Makkovik for its entire
 838 transmission period, and buoy 6 did not drift for more than 24 hours during the model run period. The results show
 839 that the model can reproduce mean regional ice drift velocities; however the model tends to underestimate high-
 840 frequency spikes in drift speeds compared to those recorded by the drift buoys 1 and 4 (Figure 27 and Figure 30).
 841 Along the track of buoy 1, the model does not capture the tidally-forced oscillations in the ice drift velocity as
 842 recorded by the buoy; this is most likely due to the inadequate spatial resolution of the NEMO 3.1 ocean current



input. For the along-track drift speeds of buoys 2 and 3, the model overestimates the increase in ice drift speeds during May 3-7 (Figure 28-Figure 29).

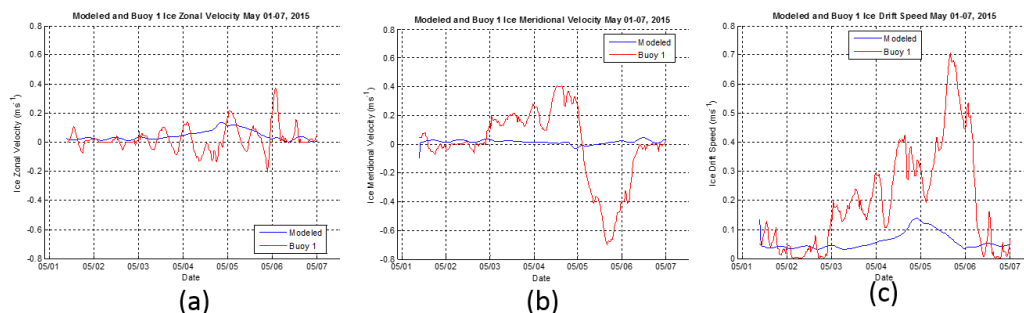


Figure 27. Modeled (blue lines) and buoy 1 measured (red lines) along-track ice drift zonal (a), meridional (b) velocities, and speeds (c) during May 1-7, 2015 offshore Labrador.

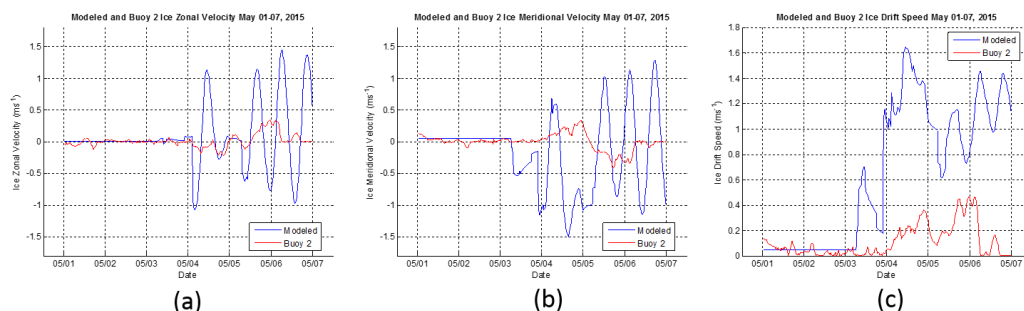


Figure 28. Modeled (blue lines) and buoy 2 measured (red lines) along-track ice drift zonal (a), meridional (b) velocities, and speeds (c) during May 1-7, 2015 offshore Labrador.

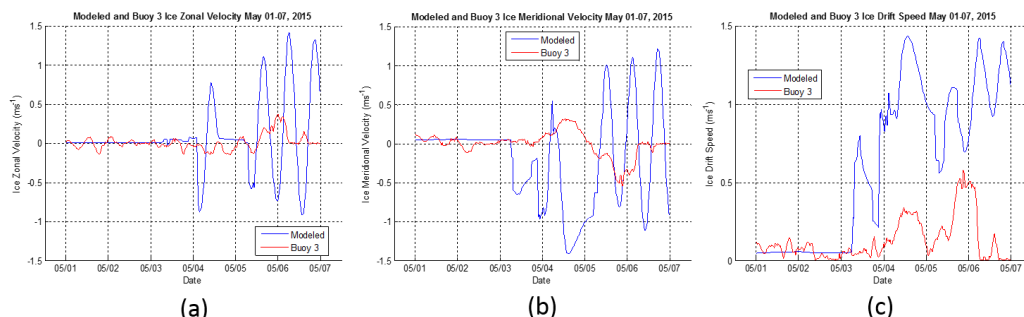
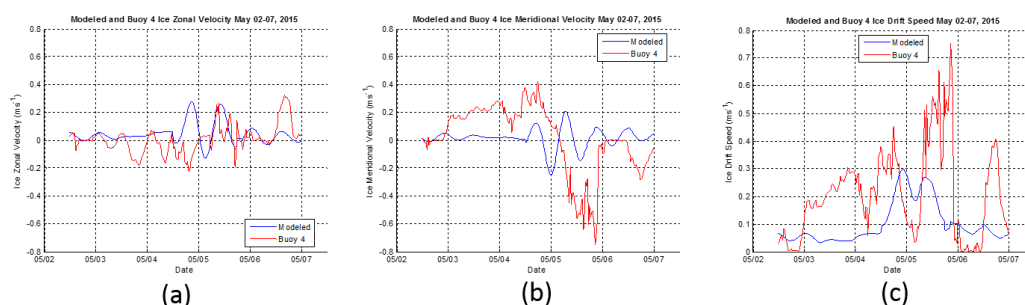


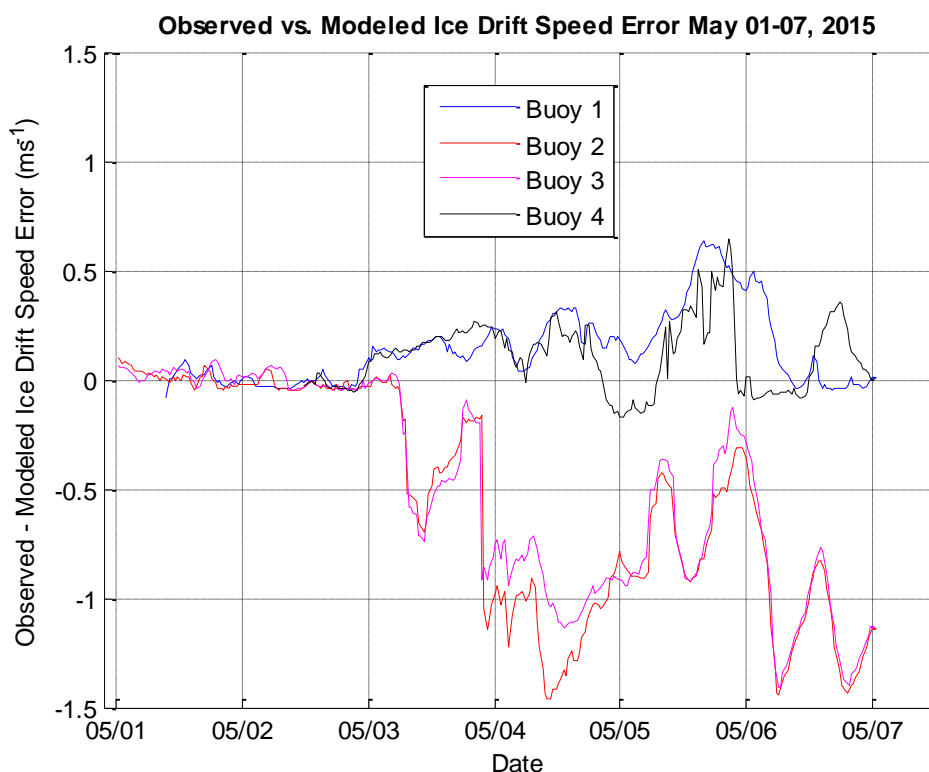
Figure 29. Modeled (blue lines) and buoy 3 measured (red lines) along-track ice drift zonal (a), meridional (b) velocities, and speeds (c) during May 1-7, 2015 offshore Labrador.



854

855 **Figure 30.** Modeled (blue lines) and buoy 4 measured (red lines) along-track ice drift zonal (a), meridional (b)
 856 velocities, and speeds (c) during May 1-7, 2015 offshore Labrador.

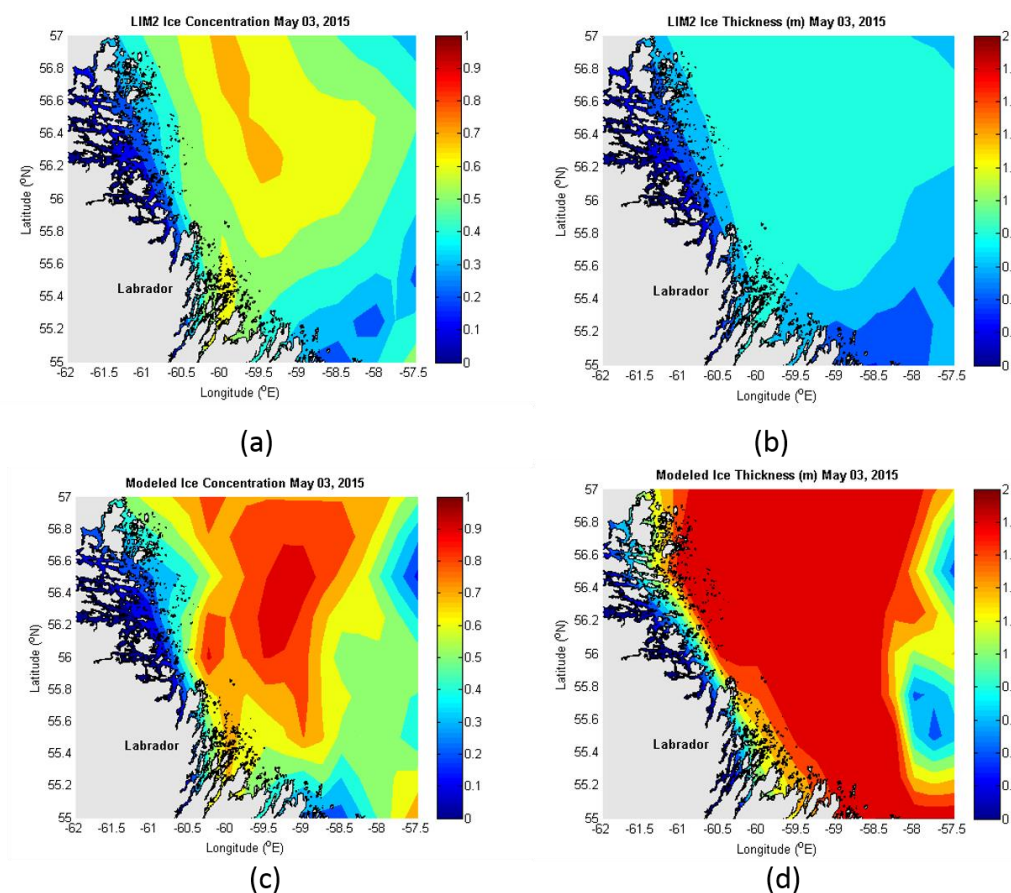
857 Figure 31 shows the observed minus modeled ice drift speed errors during May 1-7 for buoys 1-4. The buoy-
 858 recorded and modeled drift speeds were very close during May 1-3. For buoys 1 and 4, the observed-modeled drift
 859 speed error increases to 0.2-0.5 m s⁻¹ during May 3-7. For buoys 2 and 3, the observed-modeled drift speed error
 860 increases to 0.5-1.5 m s⁻¹ during this same period. These results indicate that the model is better at simulating
 861 observed ice drift speeds further offshore compared to nearshore drift speeds, as buoys 1 and 4 drifted further
 862 offshore than buoys 2 and 3 (see Figure 1). Beginning on May 3, the modeled ice velocities along the tracks of
 863 buoys 2 and 3 increase significantly over the observed buoy-tracked ice velocities. This is due to increases in the
 864 internal ice stresses, sea surface tilt forcing, and coastal boundary forcing along the nearshore tracks of buoys 2 and
 865 3 in the model.



866

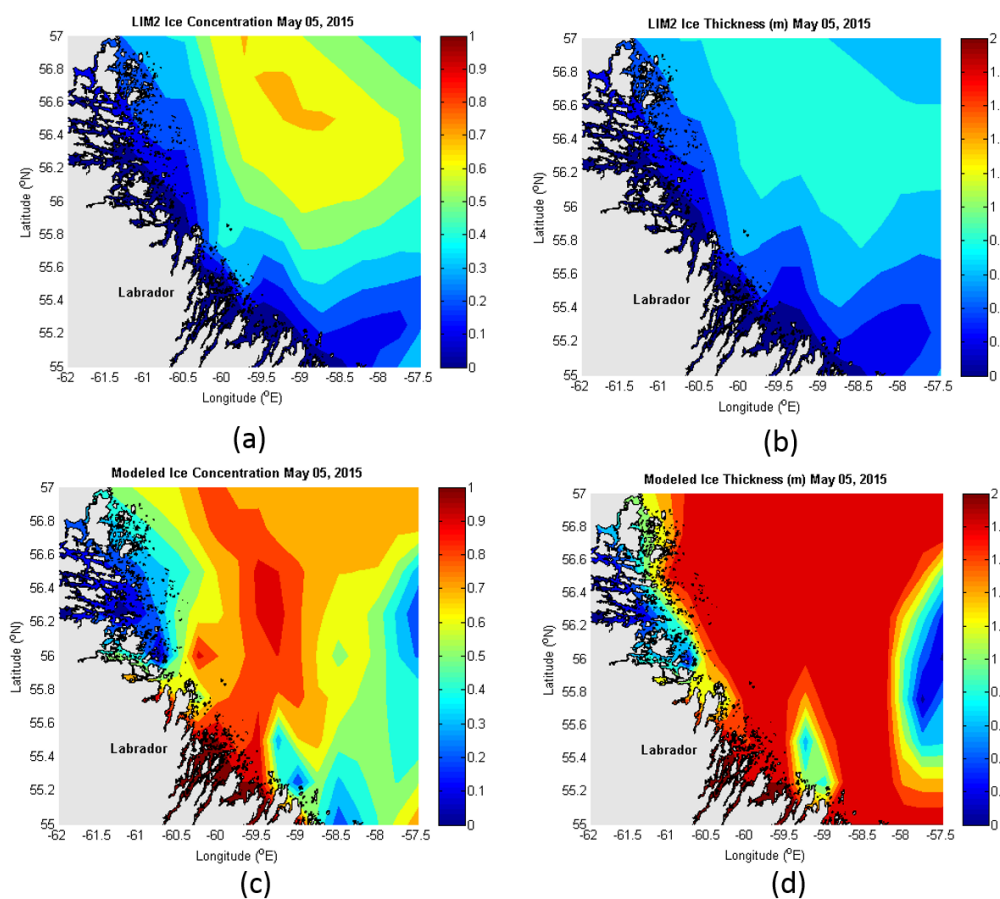
867 **Figure 31.** Observed minus modeled ice drift speeds along the trajectories of buoys 1-4 during May 1-7, 2015
 868 offshore Labrador.

869 Figure 32-Figure 34 show the LIM2 and modeled ice thickness and concentrations for the model domain for May 3,
 870 5, and 7, respectively. The model tends to overestimate ice thicknesses and concentrations across the domain;
 871 however the model does capture the fact that a tongue of higher ice concentrations develops toward the middle of
 872 the model domain.



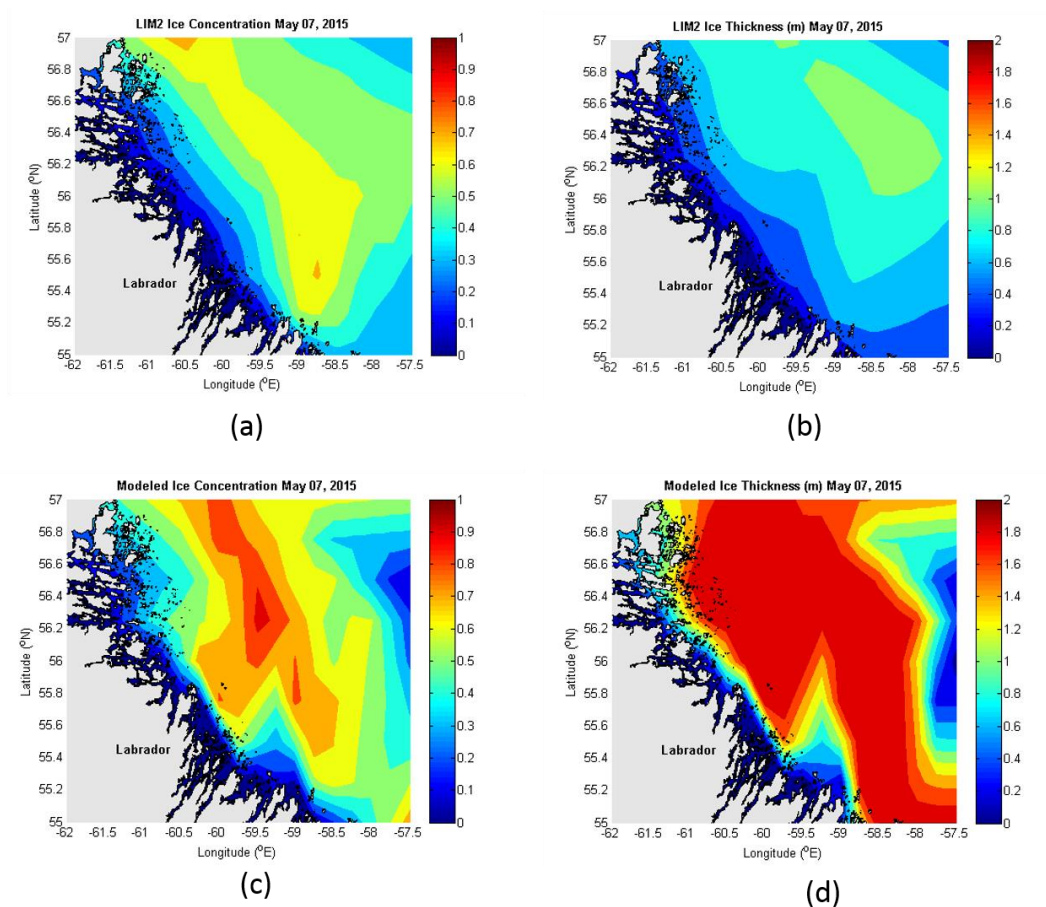
873

874 **Figure 32.** Sea ice concentration (a,c) and thickness (b,d) on May 03, 2015 03:00 UTC (00:00 AST) from LIM2
 875 data (a,b) and the thermodynamic-dynamic model presented here (c,d).



876

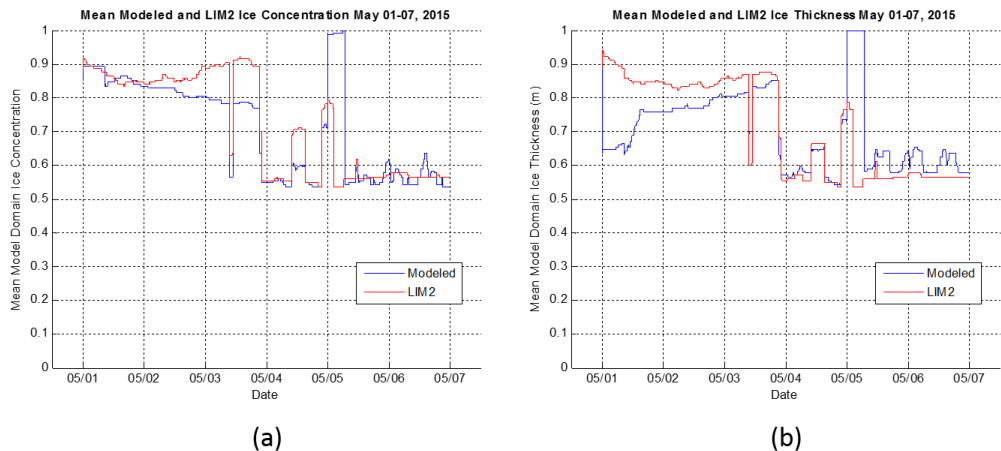
877 **Figure 33.** Sea ice concentration (a,c) and thickness (b,d) on May 05, 2015 03:00 UTC (00:00 AST) from LIM2
 878 data (a,b) and the thermodynamic-dynamic model presented here (c,d).



879

880 **Figure 34.** Sea ice concentration (a,c) and thickness (b,d) on May 07, 2015 00:00 UTC (May 06 21:00 AST) from
 881 LIM2 data (a,b) and the thermodynamic-dynamic model presented here (c,d).

882 Figure 35 shows the evolution of the mean model domain ice thickness (a) and concentration (b) during May 1-7 for
 883 the model and the LIM2 dataset.



884
885 **Figure 35.** Evolution of average ice concentration (a) and thickness (b) over the entire model domain during May 1-
886 7, 2015. The red lines represent LIM2 ice conditions, and the blue lines represent ice conditions for the
887 thermodynamic-dynamic model presented here.
888 Table 6 summarizes the mean model domain ice thicknesses and concentrations for the model and the LIM2 dataset
889 for the selected dates analyzed in this section.
890 **Table 6.** Summary of modeled vs. LIM2 model domain mean ice concentration and thickness for selected dates for
891 May 1-7, 2015 model run.

Modeled vs. LIM2 Mean Domain Ice Concentration and Thickness (Thermodynamic-Dynamic Model)				
Date	LIM2 Concentration	Modeled Concentration	LIM2 Thickness (m)	Modeled Thickness (m)
May 03	0.55	0.78	0.54	0.81
May 05	0.42	0.75	0.42	0.80
May 07	0.39	0.55	0.38	0.79

892 **4 Conclusions**

893 A model is presented in this paper which can be used to generate short-term (several days) to seasonal (months)
894 forecasts of regional ice conditions for coastal Labrador. It was shown that when the thermodynamic model was
895 used by itself for the April-May 2015 period, forecasts of the timing of the near-disappearance of ice near Makkovik
896 and Nain, Labrador were accurate to within one to four days when the model was initialized on April 1 (Figure 17).
897 For the specific locations on the land-fast ice at which the tracking buoys were originally deployed, the
898 thermodynamic model predicted the times at which the land-fast ice started to break-up accurately to within 4.7
899 hours to up to almost six days (Figure 18 and Table 4). However, these model results assumed a uniform snow cover



900 of 0.4 m on the sea ice on April 1 for the whole model domain of coastal Labrador. Given the extreme uncertainty of
901 this initial condition, it is imperative that operational use of this model utilize accurate measurements of snow cover
902 for the initialization of the model. It may be possible to hindcast initial snow depths by fitting the thermodynamic
903 model to seasonal evolutions of ice cover as documented by the CIS ice charts.

904 The thermodynamic model can be used to generate seasonal forecasts of the timing and spatial pattern of the break-
905 up of the land-fast ice along coastal Labrador. Such forecasts are important to operational planning for possible
906 future oil and gas exploration and production operations in this region, as well as vessel transport operations such as
907 those associated with the Voisey's Bay nickel mine. Access to ports near Makkovik and Nain is not possible for low
908 or non-ice class vessels prior to the break-up of the land-fast ice.

909 The coupled thermodynamic-dynamic model can be used to issue forecasts of the evolution of the coastal Labrador
910 ice cover over shorter periods of days to weeks compared to the thermodynamic-only model, which can help inform
911 the planning of ice management operations and vessel routing. The modeled ice drift speeds during May 1-7, 2015
912 were within 1.5 m s^{-1} of those measured by the tracking buoys deployed on the land-fast ice during April (Figure
913 31). Given the fact that the dynamic model does not account for ice entering or leaving the edges of the model
914 domain, the model should be run for as large an area as possible and for shorter periods, with the selected model
915 domain boundaries far away from particular locations of interest for ice forecasting. The temporal and spatial
916 resolution of the model can be adjusted by the user, with computational efficiency and model runtimes improving at
917 lower resolutions.

918 The model is most likely sensitive to a number of the thermodynamic and dynamic parameters such as the number
919 of nearest-neighbor ice particles and the smoothing length used in the SPH scheme, among others. Further study of
920 the model's sensitivity to these parameters is warranted. In addition, the thermodynamic model for prediction of the
921 onset of land-fast ice break-up does not account for the effects of wind stress. The wind speed in the current
922 thermodynamic model only affects the ice through the sensible and latent heat fluxes (Eqs. 32 and 39, respectively).
923 Future development of this model should account for the tensile stresses imposed on the offshore land-fast ice
924 boundary by the offshore component of the wind.

925 Finally, it is important to note that the results shown in this paper were generated with observed and hindcast
926 metocean data. Operational use of this model will require forecast metocean data, which will increase the errors in
927 the ice forecasts. However, the model can be reinitialized in near-real-time with the most up-to-date locally observed
928 gridded ice and metocean datasets in order to improve regional ice forecasts. Export of this model to other ice
929 environments is also an important aspect of this model development effort.

930 **Code and Data Availability**

931 Upon request to the lead author, the ice buoy drift data and model output raw data can be provided. The model code
932 is proprietary to C-CORE; however, for the review process, the model code can be made available temporarily to the



933 reviewers and journal editor. Upon request, all materials will be uploaded to a C-CORE FTP site with login details
934 provided.

935 **Author Contributions**

936 Ian Turnbull led the deployment of the ice tracking buoys, developed the model code, ran the simulations, and wrote
937 the paper. Rocky Taylor assisted with the deployment of the ice tracking buoys and helped revise the paper.

938 **Competing Interests**

939 The authors declare that they have no conflicts of interest.

940 **Acknowledgments**

941 We thank Innu Mikun Airlines of Happy Valley-Goose Bay, NL for providing safe and reliable charter aircraft
942 services for the deployment of the ice tracking buoys. The authors gratefully acknowledge core funding for the
943 Centre for Arctic Resource Development (CARD) program at C-CORE by Hibernia Management and Development
944 Company, Ltd. (HMDC), the Terra Nova Development (Suncor Energy, Inc. – Operator), and the Research and
945 Development Corporation (RDC) of Newfoundland and Labrador. Additional financial support from RDC for
946 aspects of this work is gratefully acknowledged. Finally, we thank Dr. Martin Richard of C-CORE for his helpful
947 advice on constructing the ice model. The ice drift buoy and model output datasets used in this paper can be
948 obtained by request from the corresponding author. The model computer code is proprietary to C-CORE and cannot
949 be made publicly available.

950 **References**

- 951 Canadian Coast Guard (CCG) (2013), Chapter 3: Ice Climatology and Environmental Conditions. Accessed on the
952 World Wide Web: [http://www.ccg-gcc.gc.ca/Icebreaking/Ice-Navigation-Canadian-Waters/Ice-](http://www.ccg-gcc.gc.ca/Icebreaking/Ice-Navigation-Canadian-Waters/Ice-Climatology-and-Environmental-Conditions)
953 [Climatology-and-Environmental-Conditions](http://www.ccg-gcc.gc.ca/Icebreaking/Ice-Navigation-Canadian-Waters/Ice-Climatology-and-Environmental-Conditions), March 8, 2016.
- 954 Canadian Ice Service (CIS) Weekly Digital Ice Charts (2016), Accessed on the World Wide Web:
955 [http://iceweb1.cis.ec.gc.ca/Archive/page1.xhtml?sessionId=E8B1CC6854F560205EDA89C07D6D15F7?la](http://iceweb1.cis.ec.gc.ca/Archive/page1.xhtml?sessionId=E8B1CC6854F560205EDA89C07D6D15F7?lang=en)
956 [ng=en](http://iceweb1.cis.ec.gc.ca/Archive/page1.xhtml?sessionId=E8B1CC6854F560205EDA89C07D6D15F7?lang=en), April 27, 2016.
- 957 Cooke, M.A., Demirov, E., and Zhu, J. (2014), A Model Study of the Relationship between Sea-Ice Variability and
958 Surface and Intermediate Water Mass Properties in the Labrador Sea, *Atmosphere-Ocean*, 52(2), 142-154.
- 959 Davis, C.H. (1996), Temporal Change in the Extinction Coefficient of Snow on the Greenland Ice Sheet from an
960 Analysis of Seasat and Geosat Altimeter Data, *IEEE Transactions on Geoscience and Remote Sensing*,
961 34(5), 1,066-1,073.



- 962 Ebert, E.E., and Curry, J.A. (1993), An Intermediate One-Dimensional Thermodynamic Sea Ice Model for
963 Investigating Ice-Atmosphere Interactions, *Journal of Geophysical Research*, 98(C6), 10,085-10,109.
- 964 European Center for Medium-Range Weather Forecasting (ECMWF), ERA-Interim Reanalysis, Accessed on the
965 World Wide Web: <http://apps.ecmwf.int/datasets/data/interim-full-daily/levtype=sfc/>, March 8, 2016.
- 966 Food and Agriculture Organization (FAO) of the United Nations (2015), Chapter 3 – Meteorological data. Accessed
967 on the World Wide Web: <http://www.fao.org/docrep/x0490e/x0490e07.htm>, March 8, 2016.
- 968 Fenty, I., and Heimbach, P. (2013), Coupled Sea-Ice-Ocean-State Estimation in the Labrador Sea and Baffin Bay,
969 *Journal of Physical Oceanography*, 43(5), 884-904.
- 970 Fofonoff, N.P., and Millard Jr., R.C. (1983), Algorithms for computation of fundamental properties of seawater,
971 *Unesco technical papers in marine science*, 44.
- 972 General Bathymetric Chart of the Oceans (GEBCO) (2008), Accessed on the World Wide Web:
973 http://www.gebco.net/data_and_products/gridded_bathymetry_data/, March 8, 2016.
- 974 Global Ocean 1/12° Physics Analysis and Forecast, Accessed on the World Wide Web:
975 [http://marine.copernicus.eu/web/69-interactive-](http://marine.copernicus.eu/web/69-interactive-catalogue.php?option=com_csw&view=details&product_id=GLOBAL_ANALYSIS_FORECAST_PHYS_001_002)
976 [catalogue.php?option=com_csw&view=details&product_id=GLOBAL_ANALYSIS_FORECAST_PHYS_](http://marine.copernicus.eu/web/69-interactive-catalogue.php?option=com_csw&view=details&product_id=GLOBAL_ANALYSIS_FORECAST_PHYS_001_002)
977 [001_002](http://marine.copernicus.eu/web/69-interactive-catalogue.php?option=com_csw&view=details&product_id=GLOBAL_ANALYSIS_FORECAST_PHYS_001_002), March 8, 2016.
- 978 Gutfraind, R., and Savage, S.B. (1997), Smoothed Particle Hydrodynamics for the Simulation of Broken-Ice Fields:
979 Mohr-Coulomb-Type Rheology and Frictional Boundary Conditions, *Journal of Computational Physics*,
980 134, 203-215.
- 981 Hibler III, W.D. (1979), A Dynamic Thermodynamic Sea Ice Model, *Journal of Physical Oceanography*, 9, 815-846.
- 982 Holland, M.M., Bailey, D.A., Briegleb, B.P., Light, B., and Hunke, E. (2012), Improved Sea Ice Shortwave
983 Radiation Physics in CCSM4: The Impact of Melt Ponds and Aerosols on Arctic Sea Ice, *Journal of*
984 *Climate*, 25, 1,413-1,430.
- 985 International Standards Organization Draft International Standard (ISO/DIS 19901-1) (2013), Petroleum and natural
986 gas industries – Specific requirements for offshore structures – Part 1: Metocean design and operating
987 considerations.
- 988 Khandekar, M.L. (1980), Inertial oscillations in floe motion over the Beaufort Sea – observations and analysis,
989 *Atmosphere-Ocean*, 18(1), 1-14.
- 990 König-Langlo, G., and Augstein, E. (1994), Parameterization of the downward long-wave radiation at the Earth's
991 surface in polar regions, *Meteorologische zeitschrift*, N.F.3, Jg. 1994, H.6, 343-347.
- 992 Lazier, J.R.N., and Wright, D.G. (1993), Annual Velocity Variations in the Labrador Current, *Journal of Physical*
993 *Oceanography*, 23, 659-678.



- 994 Lindsay, R.W., and Stern, H.L. (2004), A New Lagrangian Model of Arctic Sea Ice, Journal of Physical
995 Oceanography, 34, 272-283.
- 996 MacKinnon, A. (2015), The Dufort-Frankel Method. Accessed on the World Wide Web:
997 <http://www.cmth.ph.ic.ac.uk/people/a.mackinnon/Lectures/compphys/node35.html>, March 8, 2016.
- 998 Matthews, J.H., and Fink, K.K. (2004), Numerical methods using Matlab, 4th Edition, Prentice-Hall, Inc., Upper
999 Saddle River, New Jersey, USA 0-13-065248-2, 505-508.
- 1000 Maykut, G.A., and Untersteiner, N. (1971), Some results from a time dependent thermodynamic model of sea ice,
1001 Journal of Geophysical Research, 76, 1,550-1,575.
- 1002 Mitchell, A.R., and Griffiths, D.F. (1980), The Finite Difference Method in Partial Differential Equations, John
1003 Wiley, New York, USA.
- 1004 National Oceanographic and Atmospheric Administration (NOAA) (2015), General Solar Position Calculations.
1005 Accessed on the World Wide Web: <http://www.esrl.noaa.gov/gmd/grad/solcalc/solareqns.PDF>, March 8,
1006 2016.
- 1007 North American Regional Reanalysis (NARR), NCEP Reanalysis data provided by the NOAA/OAR/ESRL PSD,
1008 Boulder, Colorado, USA, from their Web site at <http://www.esrl.noaa.gov/psd/>, March 8, 2016.
- 1009 Peng, S. (1989), Application of a Simple Ice-Ocean Model to the Labrador Sea. Master of Science Thesis,
1010 Department of Meteorology, McGill University, Montreal, Quebec, Canada.
- 1011 Prinsenberg, S.J., Peterson, I.K., Holladay, J.S., and Lalumiere, L. (2011), Snow and Ice Thickness Properties of
1012 Lake Melville, a Canadian Fjord Located along the Labrador Coast, Proceedings of the Twenty-first (2011)
1013 International Offshore and Polar Engineering Conference (ISOPE), Maui, Hawaii, USA, June 19-24, 2011.
- 1014 Prinsenberg, S.J., and Yao, Q. (1999), The Seasonal Evolution of Sea Ice Cover off eastern Canada as Simulated by
1015 a Coupled Ice-Ocean Model for 1991/92 and Expected 2×CO₂ atmospheric conditions. Accessed on the
1016 World Wide Web: [http://www.bio.gc.ca/science/research-recherche/ocean/ice-
1017 glance/documents/prins05.pdf](http://www.bio.gc.ca/science/research-recherche/ocean/ice-glance/documents/prins05.pdf), March 8, 2016.
- 1018 Sayed, M., Carrieres, T., Tran, H., and Savage, S.B. (2002), Development of an Operational Ice Dynamics Model
1019 for the Canadian Ice Service, Proceedings of the Twelfth (2002) International Offshore and Polar
1020 Engineering Conference (ISOPE), Kitakyushu, Japan, May 26-31, 2002.
- 1021 Timco, G.W., and Frederking, R.M.W. (1990), Compressive Strength of Sea Ice Sheets, Cold Regions Science and
1022 Technology, 17, 227-240.
- 1023 Timco, G.W., and Johnston, M.E. (2002), Sea Ice Strength during the Melt Season. Proceedings of the 16th
1024 International Association of Hydraulic Engineering and Research (IAHR) International Symposium on Ice,
1025 Dunedin, New Zealand, December 2-6, 2002.



- 1026 Tonboe, R.T., Dybkjaer, G., and Hoyer, J.L. (2011), Simulations of the snow covered sea ice surface temperature
1027 and microwave effective temperature, *Tellus*, 63A, 1,028-1,037.
- 1028 Tsonis, A. (2002), *An Introduction to Atmospheric Thermodynamics*. Cambridge University Press 0-521-79676-8,
1029 182.
- 1030 Vale (2015), Voisey's Bay. Accessed on the World Wide Web:
1031 <http://www.vale.com/canada/EN/business/mining/nickel/vale-canada/voiseys-bay/Pages/default.aspx>,
1032 March 8, 2016.
- 1033 Water equivalent to snow ratios: DOC/NOAA/NWS (1996), *Observing Handbook Number 7, Surface Observations*
1034 part IV, Supplementary Observations, Table 2-14, 440 pp.
- 1035 Woods Hole Oceanographic Institute (2010), Humidity, Accessed on the World Wide Web:
1036 <http://www.whoi.edu/page.do?pid=30578>, March 8, 2016.
- 1037 Yao, T. (2000), Assimilating Sea Surface Temperature Data into an Ice-Ocean Model of the Labrador Sea, Canadian
1038 Technical Report of Hydrography and Ocean Sciences, 212.
- 1039 Yao, T., Tang, C.L., Carrieres, T., and Tran, D.H. (2000a), Verification of a coupled ice ocean forecasting system
1040 for the Newfoundland shelf, *Atmosphere-Ocean*, 38(4), 557-575.
- 1041 Yao, T., Tang, C.L., and Peterson, I.K. (2000b), Modeling the seasonal variation of sea ice in the Labrador Sea with
1042 a coupled multicategory ice model and the Princeton ocean model, *Journal of Geophysical Research*,
1043 105(C1), 1,153-1,165.